Available online at www.CivileJournal.org

# Civil Engineering Journal

(E-ISSN: 2476-3055; ISSN: 2676-6957)

Vol. 11, No. 03, March, 2025

# Shear Strength and Serviceability of GFRP-Reinforced Concrete Beams: A Study on Varying Reinforcement Ratios

Thar Mohammed Hamed [1*], AbdulMuttalib I. Said [1]

[1] *Department of Civil Engineering, College of Engineering, University of Baghdad, Baghdad 17001, Iraq.*

Received 16 December 2024; Revised 12 February 2025; Accepted 19 February 2025; Published 01 March 2025

**Abstract**

This study investigates the behavior of GFRP-reinforced concrete beams with varying reinforcement ratios. The experimental program consists of five concrete beams tested under a simply supported four-point bending setup with a section of (250×300) mm and a clear span of 1800 mm with a span-to-depth ratio of 2.3. The beams were reinforced longitudinally with GFRP bars with varying reinforcement ratios (ρ = 0.5, 0.9, 1.35, 1.8, and 2.25) for B1-B5, respectively. GFRP stirrups were used for the transverse direction with a spacing of 240 mm for all the beams. The results showed that raising the GFRP longitudinal reinforcement ratio to 1.35 enhanced load-carrying capacity performance and dropped at higher reinforcement ratios (1.8, 2.25) while offering better performance in controlling crack widths and deflection, which could be due to the limit of bonding with concrete. Increasing the GFRP longitudinal reinforcement ratio reduced the deflection at both service and ultimate loads with enhanced crack control. Lower reinforcement ratios of (ρ= 0.5) resulted in a brittle failure, wider cracks, and poor stiffness. Conversely, a 1.8 reinforcement ratio led to delayed crack initiation, smaller crack widths, and a balanced stiffness-to-ductility ratio being achieved. It was found that the dowel action of longitudinal GFRP bars greatly contributes to the shear strength of concrete beams, with a ratio of (ρ= 1.35) having the maximum load capacity along the tested beams. The ductility index ranged from 1.7 to 2.49. Higher reinforcement ratio beams resulted in a deeper neutral axis up to (ρ = 1.35), demonstrating improved stress distribution and reduced deformations.

*Keywords:* GFRP; Shear Strength; Dowel Action; Serviceability; Crack Width; DIC; Deflection.

## 1. Introduction

The corrosion of steel reinforcement in concrete structures has long been a critical challenge, leading to structural deterioration and increased maintenance costs. This issue has driven the development of alternative reinforcement materials with superior durability. Developments in the science of materials have positioned a composite material comprising glass fibers embedded in a polymer matrix (GFRP), which offers unique advantages over conventional steel reinforcement, including corrosion resistance [1] and reduced weight, as well as high tensile strength, making it beneficial, particularly in harsh environments, such as marine structures and water-exposed infrastructure. However, the elastic modulus of FRP is much lower than that of steel. Accordingly, it is a brittle material, and its failure occurs suddenly due to the absence of a yield point [2]. Therefore, design codes and guides suggest over-reinforced sections over the traditionally under-reinforced sections of members reinforced with steel so that concrete crushing failure mechanisms are preferred by design guides and codes, including the ACI 440.1R-15 [3].

The bonding strength of GFRP bars to concrete needs to be investigated, and therefore, adjustments in design codes are crucial to providing relations that are considered in reinforcement detailing [4], which could affect the dowel action.

* Corresponding author: dhar.hamid2201m@coeng.uobaghdad.edu.iq

http://dx.doi.org/10.28991/CEJ-2025-011-03-04

The ACI code does not consider the GFRP in the compression region of the beam because of its limitations. However, findings suggest that the compressive strength of GFRP bars can be reasonably estimated to be approximately 35% of their tensile strength [5]. FRP bars exhibit lower capacity to resist compressive forces than tensile forces due to their lower modulus of elasticity relative to steel reinforcement bars [6].

Several factors, including the contribution of stirrups, aggregate interlock, and longitudinal reinforcement, impact the shear strength of concrete beams. Stirrups tie the two sides of the diagonal cracks caused by vertical shear forces and longitudinal stress in the shear zone. Aggregate interlock enhances shear strength by resisting shear through friction and interlocking along the crack surfaces, while longitudinal reinforcement acts as dowels that transfer forces across the cracks. The bond strength properties of GFRP stirrups differ from those of steel stirrups, which affect the shear strength as stirrups transfer tensile forces to the surrounding concrete through the bond, effectively restricting crack openings and maintaining dowel action and aggregate interlock. However, during the manufacturing and bending of GFRP stirrups, the bent portions exhibit reduced strength compared to the straight portions [7]. For this, design codes include strength reduction factors for GFRP stirrups. The mechanical behavior of steel stirrups differs significantly from that of GFRP stirrups. Steel stirrups exhibit an elastic-plastic stress-strain response. Initially, they deform elastically under shear forces, and upon reaching the yield strength, they transition into a plastic deformation phase. This yielding phase redistributes stresses among adjacent stirrups, providing ductility and allowing the beam to withstand loads beyond its design limit without sudden failure. In contrast, GFRP follows a linear elastic stress-strain curve and lacks a yielding phase [8]. Once the ultimate stress of the GFRP rebar is exceeded, sudden failure will occur. This brittle behavior makes understanding and accounting for the unique properties of GFRP essential for effective design and performance. Strengthening of concrete by FRP increased load capacity while reducing deflection [9]. In addition, it contributes to increased ductility for repeated load [10], highlighting GFRP's suitability for enhancing cyclic load performance. Table 1 presents a summary of the literature review.

**Table 1. Summary of the Literature Review**

| Study By | Specimens Details | Key Findings |
|---|---|---|
| Wegian et al. (2005) [11] | 7 beams, GFRP/CFRP longitudinal, steel stirrups | GFRP beams showed larger curvatures after cracking due to lower modulus; CFRP beams performed better. |
| Ashour (2005) [12] | 12 beams, no stirrups | GFRP rupture caused flexural failure in under-reinforced beams; over-reinforced beams failed in shear. |
| Tavares et al. (2008) [13] | 6 beams, GFRP longitudinal, steel stirrups | GFRP beams had similar flexural capacity to steel beams but with more cracks and reduced stiffness. |
| Nguyen-Minh et al. (2011) [14] | 12 beams, GFRP/steel longitudinal, steel stirrups | Increasing the GFRP ratio improved stiffness and reduced deflection; failure differed from steel beams. |
| Kalpana & Subramanian (2011) [15] | 9 beams, GFRP longitudinal, steel stirrups | GFRP beams displayed linear elastic behavior and lower crack width with high-strength concrete. |
| Maranan et al. (2015) [16] | 3 beams, GFRP/steel stirrups, no stirrups | Stirrups improved shear capacity; GFRP stirrups showed brittle failure. |
| Said et al. (2016) [17] | 10 beams, GFRP longitudinal, and stirrups | Decreased stirrup spacing significantly improved shear strength and controlled crack propagation. |
| Kaszubska et al. (2017) [18] | 7 beams, T-shaped GFRP longitudinal, no stirrups | Beams with two-layer reinforcement exhibited higher shear strength due to dowel action. |
| Krasniqi et al. (2018) [19] | 9 beams, steel/GFRP longitudinal | GFRP beams exhibited wider cracks and higher deflections than beams of steel reinforcement. |
| Menam et al. (2021) [20] | 8 beams, steel/GFRP longitudinal | GFRP's lower modulus influenced shear failure; the reinforcement ratio had a notable shear effect. |
| Moawad & Fawzi (2021) [21] | 6 beams, partially/fully GFRP reinforced | Increased GFRP ratio improved flexural strength; concrete compressive strength significantly mattered. |
| Yuan et al. (2022) [22] | 8 beams, GFRP stirrups | CW-GFRP stirrups improved shear capacity and avoided bond/slip failure. |
| Ali & Said (2023) [23, 24] | 5 beams, GFRP reinforced, w and w/o openings | Horizontal openings result in higher $P_u$; one opening causes $P_u$ to increase compared to 2 adjacent openings. |
| AbdulMuttalib et al. (2024) [25, 26] | 6 beams, GFRP stirrups | Reduced stirrup spacing enhanced ductility and crack control; shear failure was delayed. GFRP bars in the compression zone had a negligible effect |
| Mohammed & Said (2024) [27, 28] | 5 beams, steel/GFRP longitudinal/stirrups | GFRP stirrups led to lower shear capacity than steel, but beams showed adequate crack control. Results validated by simulated model |
| Rasheed et al. (2024) [29] | 3 slabs, steel/GFRP reinforced | (20%-40%) GFRP replacement reduced cracking load and stiffness. Flexural mode shifted to shear mode with higher GFRP ratios. |
| Zhao et al. (2024) [30] | 6 beams, GFRP stirrups | Increasing stirrup spacing reduced shear capacity and changed failure mode. |

According to ACI 440.11-22 [31], a rupture strength reduction coefficient $C_E$ (Equation 1) accounts for long-term environmental exposure, which can reduce the tensile strength of FRP bars. The magnitude of this reduction depends on the material properties and the type and severity of environmental conditions. For steel stirrups, ACI 318-19 [32] does not apply a strength reduction factor for bent portions, as steel is an isotropic and ductile material, and the yield strength ($f_y$) is used directly for shear strength calculations, allowing stress redistribution at the bends, thereby preventing localized failure. In contrast, GFRP is an orthotropic material, meaning its mechanical properties vary with the direction of applied loads. As a result, the bent portions' effect of bend geometry on the tensile strength of reinforcement varies significantly between steel and GFRP stirrups. GFRP stirrups experience a significant reduction in tensile strength due to a combination of bending stresses, fiber misalignment, and stress concentrations, $f_{fb}$ (Equation 2) by ACI 440.11-22 [31] is presented to reduce strength due to this bent portion. The failure mode is brittle, as the fibers cannot effectively redistribute stresses once localized failure initiates. When GFRP bars are bent to form stirrups, the outer fibers at the bend radius experience tensile stress while the inner fibers undergo compression. This creates stress concentrations that weaken the bar, with smaller bend radii exacerbating this effect. Increasing the bend radius can help reduce stress concentrations and minimize tensile strength reduction to mitigate this issue. Unlike GFRP stirrups, steel stirrups do not suffer from this reduction, maintaining their shear resistance and ductility regardless of bend geometry.

$$f_{fu} = C_E \left(f_{fu}{}^*\right) \tag{1}$$

$$f_{fb} = \left(\left(0.05 \frac{r_{bend}}{d_{bar}} + 0.3\right) f_{fu}\right) \leq f_{fu} \tag{2}$$

Digital Image Correlation (DIC) emerged as a powerful non-contact optical measurement technique enabling detailed displacement and strain measurements, which capture the entire deformation behavior of a specimen and offer a comprehensive understanding of its mechanical performance. The application of DIC in testing concrete members gives the ability to monitor crack initiation, propagation, and the development of strains. The technique involves high-resolution cameras and advanced image-processing algorithms. DIC monitors the movement of a randomly distributed speckle pattern, which is required to allow the software to correlate the images, taking the speckle as a datum point to compare its location between different load stages. Reu (2014) [33] explored speckle pattern design, focusing on speckle size measurement and its implications for spatial resolution and accuracy. Reu (2014) [33] highlighted the risks of aliasing in speckle patterns, making it challenging to render accurate size measurements, compromising reliability, and linking small speckles to better resolution while cautioning against minimal patterns that could introduce noise. Each subset should contain (2–3) speckles to provide appropriate size for accurate measurements. Jones & Iadicola (2018) [34] provides an extensive framework for conducting reliable and accurate DIC measurements. Details of the setup requirements and critical parameters for achieving high-fidelity results are of great importance, such as the quantity of interest (QOI) (displacement, strain, crack pattern, and shape measurements), the portion of a specimen operated on by DIC analysis, the region of interest (ROI), and the optimal stand-off distance (SOD) between the camera and the test specimen's surface.

Several studies have investigated the behavior of GFRP-reinforced beams, with higher ratios generally improving post-cracking stiffness and reducing deflection [11, 15], which is important because of the overall lower stiffness of GFRP than steel, primarily due to the inherently lower stiffness of polymer fibers [35]. However, excessive reinforcement ratios do not enhance shear strength proportionally due to bond limitations and inefficiency in dowel action [18]. Research indicates that reducing stirrup spacing enhances shear strength and delays failure [30]. GFRP stirrups, while effective in resisting shear, exhibit brittle failure characteristics, unlike steel stirrups, which allow for stress redistribution [16, 27]. Existing research does not fully quantify the interaction between dowel action and shear strength for GFRP-reinforced beams. The serviceability criteria need to be investigated more for varying GFRP reinforcement ratios and optimum reinforcement ratios. Serviceability requirements may become the controlling factor in the design of FRP-reinforced concrete and should be re-evaluated [36]. Most studies examine GFRP ductility with a fixed reinforcement ratio, lacking a comparative evaluation across multiple ratios. Prior research highlights discrepancies between experimental and theoretical shear predictions at high reinforcement ratios.

A systematic research framework to evaluate the performance of GFRP-reinforced concrete beams under different reinforcement ratios and testing configurations. The methodology includes detailed phases, ranging from material preparation to data analysis, ensuring a comprehensive investigation of structural behavior. Figure 1 illustrates the research methodology framework, outlining the sequential stages of the experimental program, materials, testing setup, and result analysis.

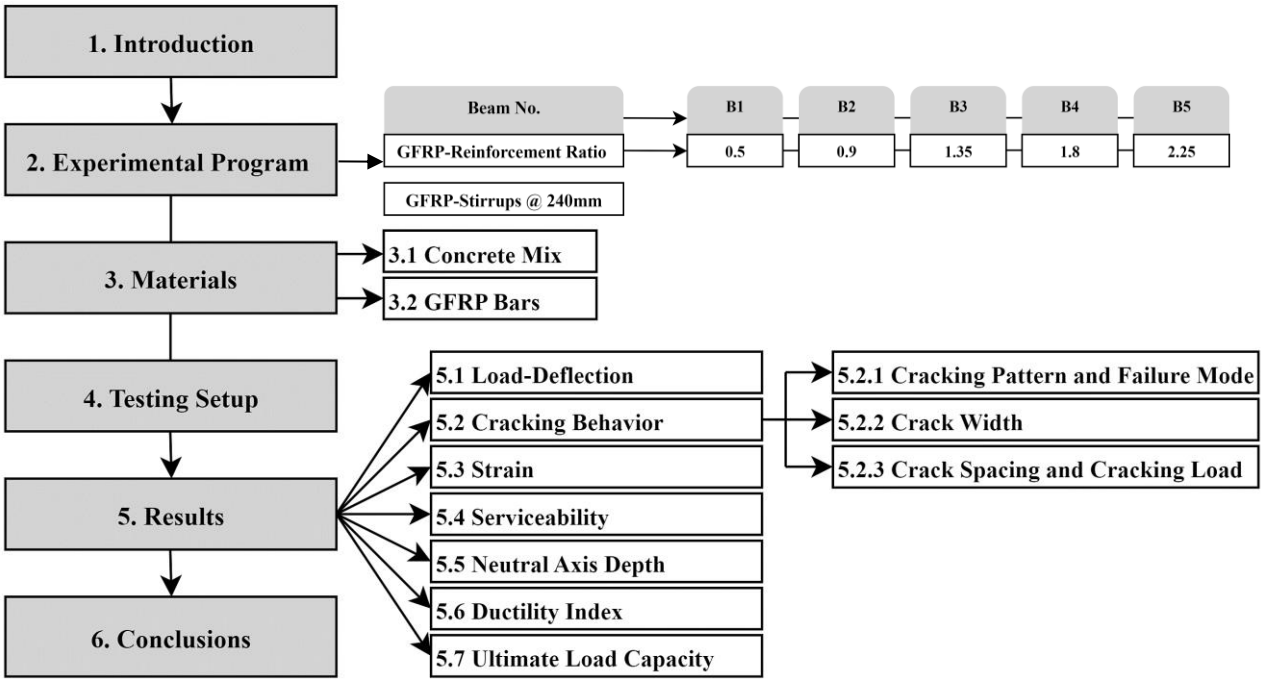


**Figure 1. Research methodology framework**

## 2. Experimental Program

The experimental program consists of five concrete beams (250×300 mm), with a clear span of 1800 mm and a shear span to effective depth ratio of 2.3, as shown in Figures 2 and 3. The beams were reinforced longitudinally with GFRP bars with a reinforcement ratio of (0.5, 0.9, 1.35, 1.8, and 2.25) for (B1, B2, B3, B4, and B5), respectively. All beams were reinforced with 8 mm GFRP stirrups (200×250 mm @ 240 mm for transverse reinforcement) and tested for a 4-point bending setup. The compressive strength of the used concrete is 40 MPa. GFRP bars of 8 mm diameter for B1 and 12 mm diameter for the other four beams are used for longitudinal tensile reinforcement, as shown in Table 2.

**Figure 2. GFRP reinforcement**

**Table 2. Beams reinforcement**

| Beam Designation | Transverse Reinforcement | | Longitudinal Reinforcement | | |
|---|---|---|---|---|---|
| | $Ø_{st}$ (mm) | S (mm) | $Ø_{bar}$ (mm) | No. of bars | $\rho_f/\rho_{fb}$ |
| B 1 | 8 GFRP | 240 (d) | 8 | 2 | 0.5 |
| B 2 | | | 12 | 2 | 0.9 |
| B 3 | | | 12 | 3 | 1.35 |
| B 4 | | | 12 | 4 | 1.8 |
| B 5 | | | 12 | 5 | 2.25 |

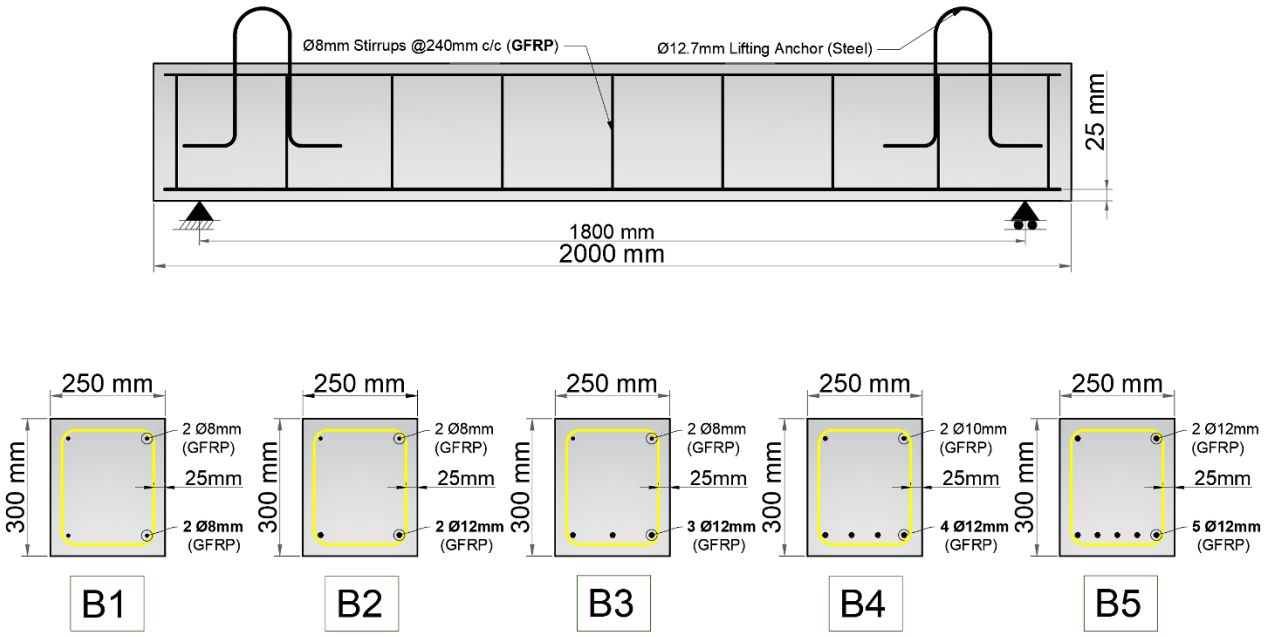


**Figure 3. Beams sections**

## 3. Materials

### 3.1. Concrete Mix

Ready-Mix Concrete (RMC) was used for its consistency and quality control. The compressive strength of the concrete mixture is (C40/50) measured at 28 days. The mixing proportions (per cubic meter) of the mixing materials and concrete properties are illustrated in Table 3. The mix contains Cement of (CEM) 42.5R (450 kg/m³) classified according to EN 197-1:2011 [37], crushed gravel aggregate (950 kg/m³) with a maximum size aggregate of (20 mm), with a size of (4.75 to 19 mm) according to ASTM C33/C33M-18 [38] and sand (850 kg/m³) within the limits of ASTM C33/C33M-18 [38], and water (160 L/m³) with a water-cement ratio (w/c) of 0.35, in addition to superplasticizer (4 L/m³), used to improve the workability and flowability of the concrete mix without reducing the strength of concrete (increasing the w/c). The mechanical properties of concrete (Compressive Strength, Tensile Strength, Modulus of Rupture, and Young's Modulus) can define how concrete responds to forces and stresses. The average compressive strength of concrete was obtained through three cylindrical samples of (150×300) mm per ASTM C31/C31M-21a [39] and tested according to ASTM C39/C39M-21 [40]. Also, three samples (cubes) of (150×150×150) mm as per EN BS 12390-2:2019 [41]. And tested according to BS EN 12390-3 [42]. The compressive strength results were 39.5 MPa and 50 MPa for cylindrical and cubical concrete samples, respectively. As for tensile strength, two cylinders were tested for splitting according to ASTM C496/C496M-17 [43] (Equation 3). And one sample for Young's modulus (ASTM C469/C469M-22) [44] (Equation 4). For flexural strength, three prisms (100×100×490 mm) were prepared (BS EN 12390-5:2009) [45] (Equation 5). All of the specimens were cured for 28 days. All test results of the mixture are summarized in Table 4.

$$T = \frac{2P}{\pi L d} \quad (3)$$

$$E_c = \frac{(S2-S1)}{(\varepsilon 2-\varepsilon 1)} \quad (4)$$

$$f_{cf} = \frac{3(F)(L)}{2(d1)(d2^2)} \quad (5)$$

**Table 3. Concrete mix quantities**

| Material | Cement | Gravel | Sand | Water | w/c | Superplasticizer |
|---|---|---|---|---|---|---|
| Quantity per 1m$^3$ | 450 kg | 950 kg | 850 kg | 160 L | 0.35 | 4 L |

**Table 4. Materials tests results**

| Test | Specimen 1 | Specimen 2 | Specimen 3 | Average | | | | |
|---|---|---|---|---|---|---|---|---|
| $\mathbf{f'_c}$ Compressive Strength (MPa) | 43.3 | 38.4 | 36.7 | 39.5 | | | | |
| $\mathbf{f_{cu}}$ Compressive Strength (MPa) | 50.0 | 53.9 | 46.2 | 50.0 | | | | |
| **T** Tensile Strength (MPa) | 3.4 | 3.3 | - | 3.35 | | | | |
| $\mathbf{f_{cf}}$ Modulus of Rupture (MPa) | 4.63 | 4.37 | 4.46 | 4.48 | | | | |
| $\mathbf{E_c}$ Young's Modulus (MPa) | 26851 | - | - | 26851 | | | | |
| Cement Classification | CEM 1 42.5R-SR- Type V | | | | | | | |
| Superplasticizer | DCP-Hyperplast PC175 | | | | | | | |
| **Coarse Aggregate [Opening mm]** | 25 | 19 | 9.5 | 4.75 | 2.36 | | | |
| %Passing Limit [4.75-19] mm | 100 | 90-100 | 20-55 | 0-10 | 0-5 | | | |
| %Passing Test Results | 10 | 92.3 | 27.3 | 2.1 | | | | |
| **Fine Aggregate [Opening mm]** | 9.5 | 4.75 | 2.36 | 1.18 | 0.6 | 0.3 | 0.15 | 0.075 |
| %Passing Limit | 100 | 95-100 | 80-100 | 50-85 | 25-60 | 5-30 | 0-10 | 0-5 |
| %Passing Test Results | 100 | 92.3 | 81.8 | 62.6 | 48.3 | 24.3 | 5.0 | 3.1 |

The particle size distribution of the aggregate used in the concrete mix shows a gravel size of (19-4.75) mm with sand that is within permissible limits, with a deviation at 4.75 mm sieve opening as per ASTM C33-33M-18 as shown in Figures 4 and 5.

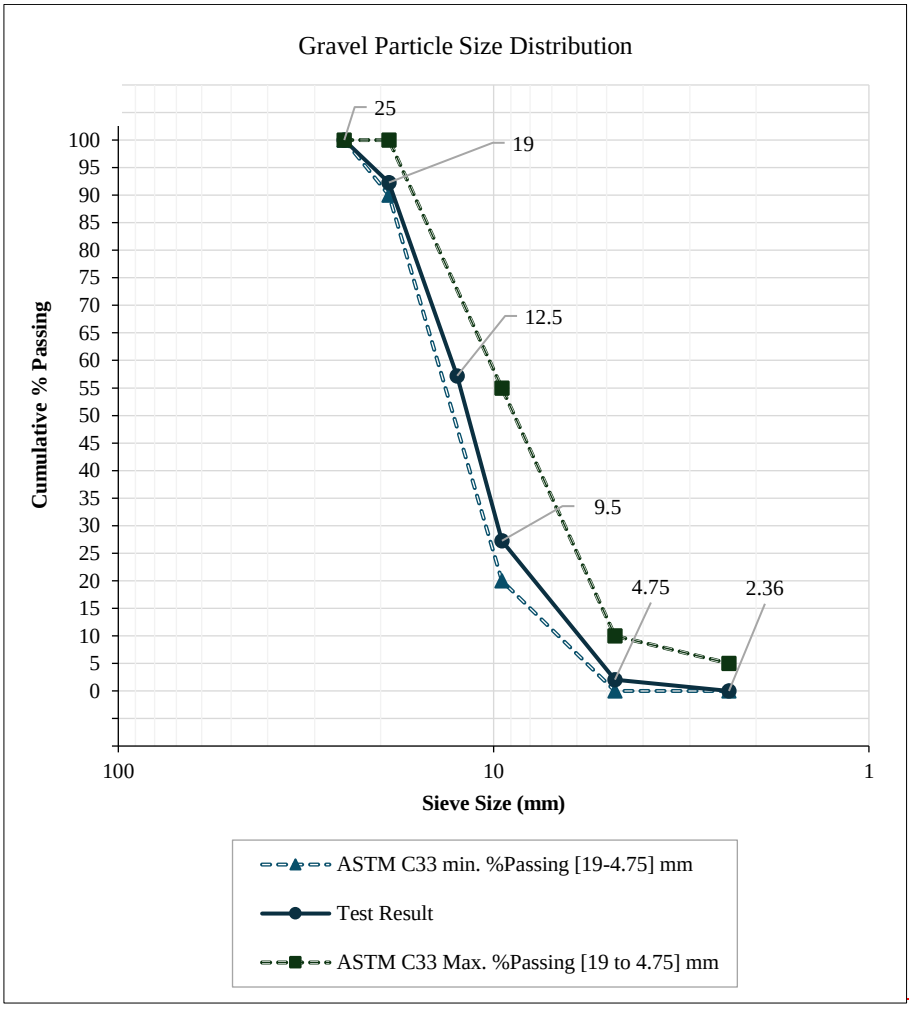


**Figure 4. Gravel particle size distribution**

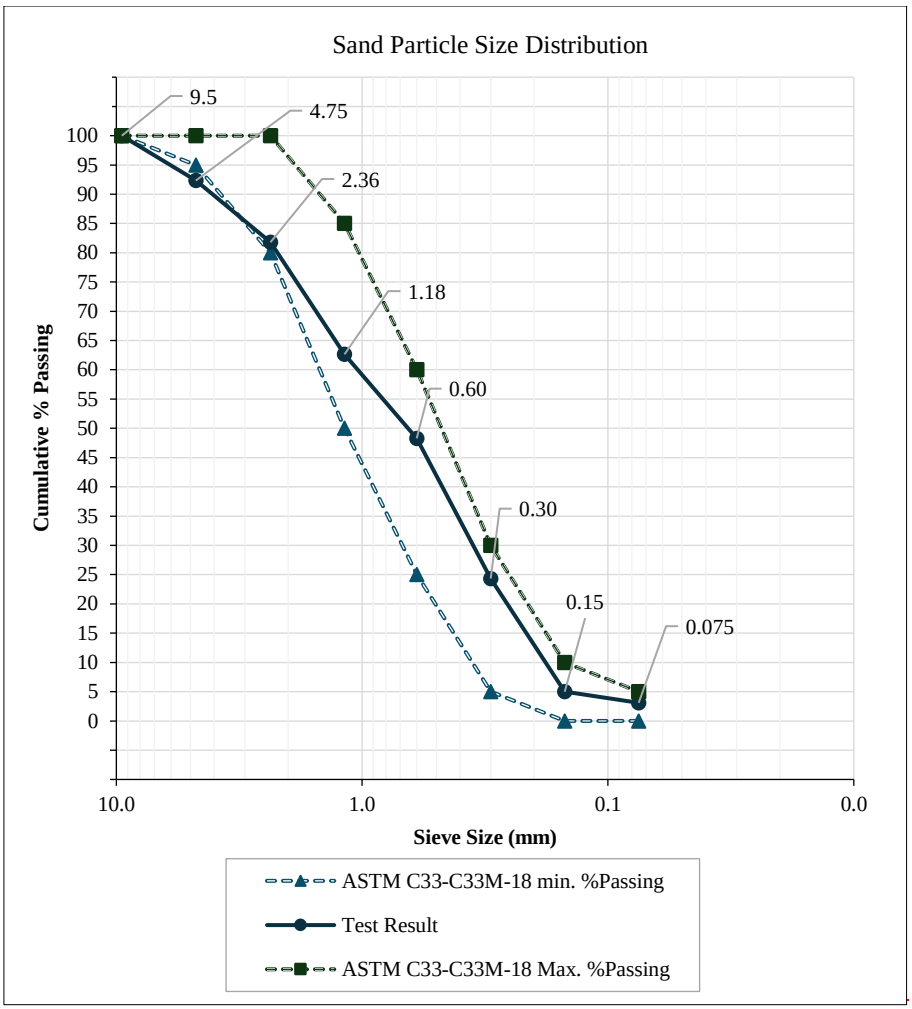


**Figure 5. Sand particle size distribution**

## 3.2. GFRP Bars

The tensile strength GFRP bars were tested per ASTM D7205/D7205M [46]. Testing required anchors to grip the bars in the testing machine during testing. Iron hollow tubes were used as anchors with epoxy (DCP Quickmast 105) applied to attach the bars to the couplers. The tested GFRP bars have a length of 980 mm and a diameter of 8 mm and 12 mm, with the tubes being 300 mm in length. Figure 6 shows the frame made to prepare the test bars. The tensile strength and elastic modulus for 8 mm and 12 mm diameter GFRP bars, in addition to the actual diameter, are shown in Table 5, with the specific gravity determined from the mass of bars in air and submerged in water. The specific gravity ranged from 2.0 to 2.1.

**Figure 6. GFRP bars tensile test**

**Table 5. GFRP bars test results**

| No. | Nominal Diameter (mm) | Specific Gravity G | Actual Diameter (mm) | Ultimate Stress (MPa) | Ultimate Strain (%) | Modulus of Elasticity (MPa) |
|---|---|---|---|---|---|---|
| 1 | 8 | 2.0 | 7.70 | 1217.6 | 2.4 | 49698 |
| 2 | 8 | 2.018 | 7.67 | 1074.4 | 2.2 | 48836 |
| 3 | 8 | 2.037 | 7.63 | 1132 | 2.3 | 49217 |
| 4 | 12 | 2.09 | 11.24 | 1310 | 2.6 | 51603 |
| 5 | 12 | 2.1 | 11.22 | 1346 | 2.5 | 50660 |
| 6 | 12 | 2.072 | 11.33 | 1281 | 2.3 | 51329 |

## 4. Test Setup

The rebar cage is prepared with strain gauges attached to it and tested to be ready for ready-mix concrete to be poured into plywood molds. All beams were cast from the same batch and cured under identical conditions. The tested beams were stored in a controlled laboratory environment, and standard curing procedures were followed to ensure uniformity across specimens. The testing frame is prepared with a loading beam and support points optimized for the physical properties of the beams, loading locations, and supporting conditions of a four-point load test setup, using a test frame with a manual hydraulic jack and an electrical hydraulic jack used throughout the test (Figure 7). A data acquisition system (DAQ) is used to collect and record the test data at a sample rate of 80 Hz, a load cell (50 tons) to record the applied load, and linear variable displacement transformers (LVDTs) are used for deflection readings and strain gauges. The (DAQ) acquisition data is processed and stored using (LabVIEW) software. The digital image correlation (DIC) speckle pattern dot size of (2-3) mm for optimal pattern quality and application practicality, applied on the rear face of the beam, enabled more detailed observations of the tested beam behavior, including the deflection profile, and provided a clear visualization of cracking propagation and pattern, using (Zeiss Inspect Correlate) software, and images captured using a digital camera every (5 seconds) during the test. Crack width can give insights to help understand and evaluate the behavior of tested beams with different reinforcement configurations. As such, a crack-width camera device was used to record the crack details, and data was recorded several times during loading. The loading setup is illustrated in Figure 7.

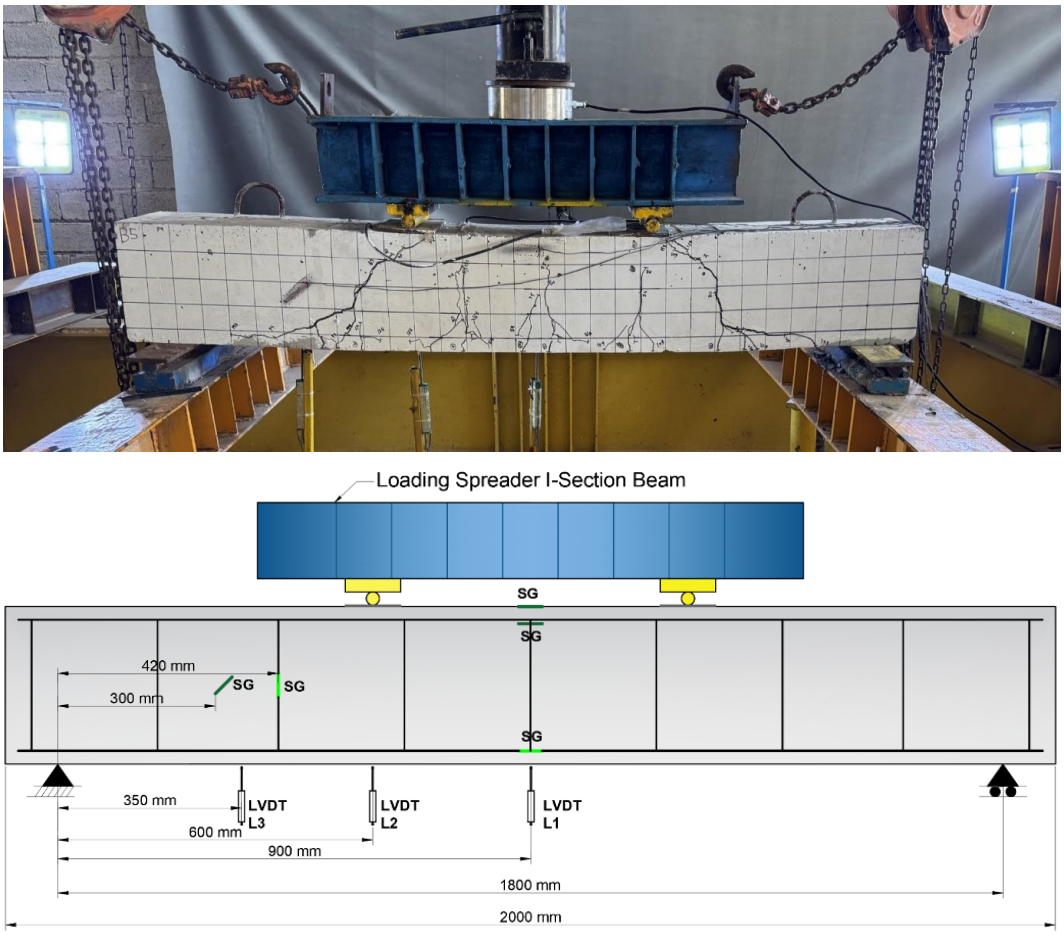


**Figure 7. Testing Setup**

# 5. Results

## 5.1. Load-Deflection

Because GFRP has a lower modulus of elasticity than steel, structural elements reinforced with GFRP generally experience increased deflections when subjected to loading [47]. The load-deflection behavior was analyzed using data obtained from LVDT and DIC techniques. Both LVDT and DIC readings show similar trends in load-deflection behavior, as shown in Figure 8. B1 (ρ=0.5) exhibits the least stiffness (shallowest slope in the elastic region) and fails at a lower ultimate load than other beams with large deflection at relatively low loads, demonstrating poor structural performance and the lowest ductility index, indicating brittle failure. B2 (ρ=0.9) slightly improved the stiffness compared to B1 but was still less stiff than the beams with higher reinforcement ratios with a moderate increase in ultimate load capacity compared to B1. B3 (ρ=1.35) represents a balance between stiffness and ductility. Achieves a significantly higher ultimate load and sustains more considerable deflections before failure, with smooth transitions without sudden failure. B4 (ρ=1.8) exhibits higher stiffness and load capacity. It shows limited deflection at lower load levels, with the transition from elastic to plastic behavior being more gradual. B5 (ρ=2.25) showed the highest stiffness and load-carrying capacity, maintaining stable deflection until very high loads, demonstrating improved energy absorption and deformation capacity. The deflection corresponding to 65% of the ultimate load (Δ@0.65Pu) varies but not significantly, showing similar initial stiffness before reaching peak strength. The deflection values of beams 1-5 are presented in Table 6.

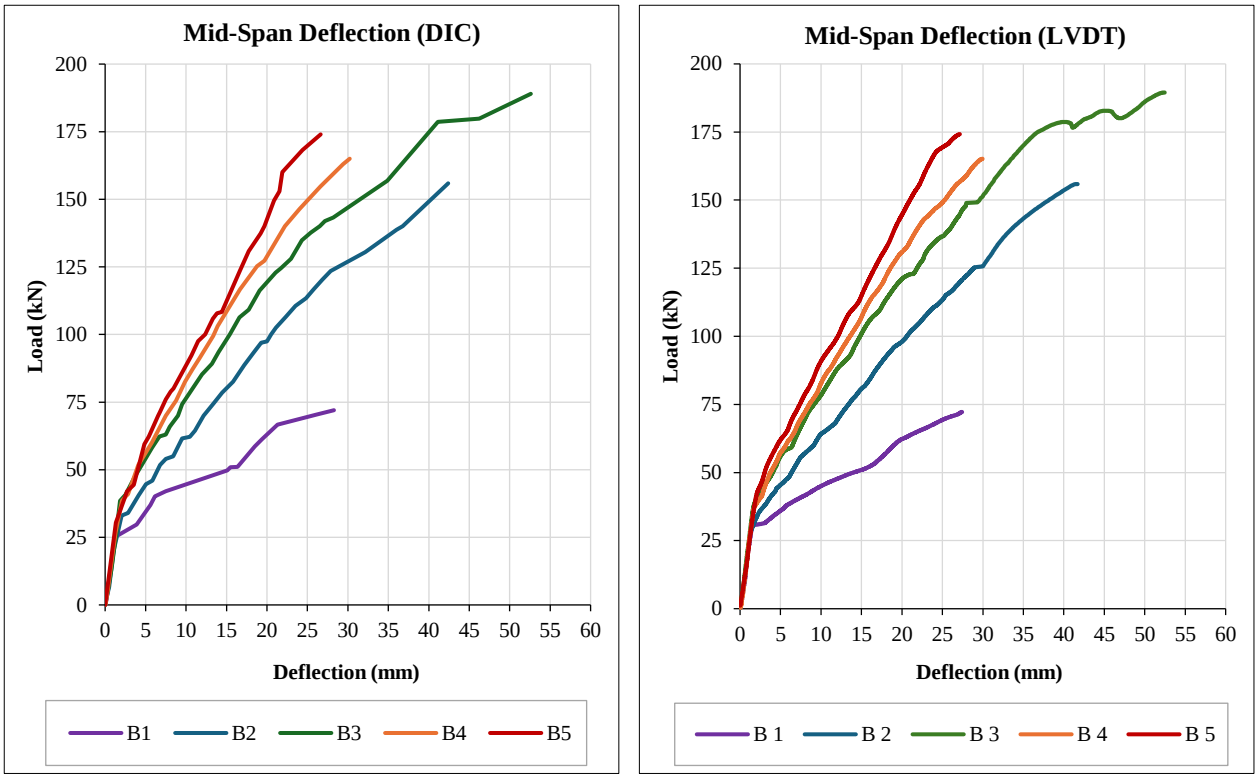


**Figure 8. Load-deflection**

**Table 6. Deflection**

| Beam No. | B1 | B2 | B3 | B4 | B5 |
|---|---|---|---|---|---|
| **Δ@0.65$P_u$ (mm)** | 11.3 | 20.9 | 21.5 | 15.1 | 14.8 |
| **Δ@$P_u$ (mm)** | 28.3 | 42.4 | 52.6 | 30.2 | 26.6 |

At service load (0.65$P_u$), the deflection behavior of the beams varied significantly based on their reinforcement ratios. Beam B1 exhibited the smallest deflection of 11.3 mm. However, with a reduction of ductility, as the beam could not sustain significant deformations, in contrast, B2, with a higher reinforcement ratio of 0.9, showed a deflection of 20.9 mm, reflecting an improvement in ductility. B3 displayed the largest deflection at service load, with 21.5 mm, indicating a balance between stiffness and ductility. B4 and B5, with reinforcement ratios of 1.8 and 2.25, respectively, showed lower deflections of 15.1 mm and 14.8 mm. This reduction in deflection reflects the increasing stiffness as reinforcement ratios rise, but it also highlights the corresponding lower ductility index. At the ultimate load ($P_u$), the differences in deflection became even more pronounced. Beam B1 had the lowest deflection of 28.3 mm, which aligns with its limited reinforcement and inability to deform significantly under high loads. Beam B2, with a deflection of 42.4 mm, demonstrated improved ductility over B1, and Beam B3 achieved the highest deflection of 52.6 mm, underscoring its

superior ability to absorb energy and deform under load. Beams B4 and B5, however, showed lower deflections of 30.2 mm and 26.6 mm, respectively. These results indicate that higher reinforcement ratios increase stiffness but reduce the beams' capacity to deform, with Beam B5 exhibiting the highest stiffness but the least ductile behavior.

## 5.2. Cracking Behavior

### 5.2.1. Crack Pattern and Failure Mode

The cracking behavior and failure modes were observed under increasing loads. The crack pattern represented in Figure 9 revealed a distinct crack formation. The beams primarily displayed a combination of flexural and flexural-shear failure modes, as illustrated in Table 7, with fewer cracks for the under-reinforced beam (B1). In contrast, beams with higher crack counts exhibited flexural-shear behavior, where additional cracks formed outside the point load locations, often sloping towards the supports. These cracks showed variations in shape, with some transitioning from straight to concave or sloping patterns, with a near-simultaneous failure in the two shear spans for the (B3) beam, causing leverage in the ultimate load capacity. (B1) with a reinforcement ratio of 0.5, failure was predominantly flexural, characterized by straight cracks with rapid widening under increased loads, cracks initiated in the mid-span under bending loads, propagating vertically. (B2) showed a combination of flexural and shear failure; initial cracks were vertical and appeared in the bending region, but with increasing load, additional cracks developed towards the supports, sloping slightly, characteristic of flexural-shear behavior. Also, (B3) displayed flexural-shear failure, as cracks began vertically in the bending zone, extending with sloping patterns towards the supports, indicative of shear influence alongside flexural stresses. (B4) displayed similar flexural-shear behavior, with cracks initiated in the mid-span but evolved with significant sloping towards the supports, suggesting a combination of bending and shear stresses contributing to failure. (B5) demonstrated a flexural-shear failure mode. The crack pattern included vertical bending cracks that extended and sloped towards the supports as load increased, resulting in combined flexural and shear failure. The crack patterns of B1 to B5 are shown in Figure 9. Table 7, details the number and nature of cracks for each specimen, along with the observed failure mode, the number of cracks and the crack branches, and the failure mode of the beams.

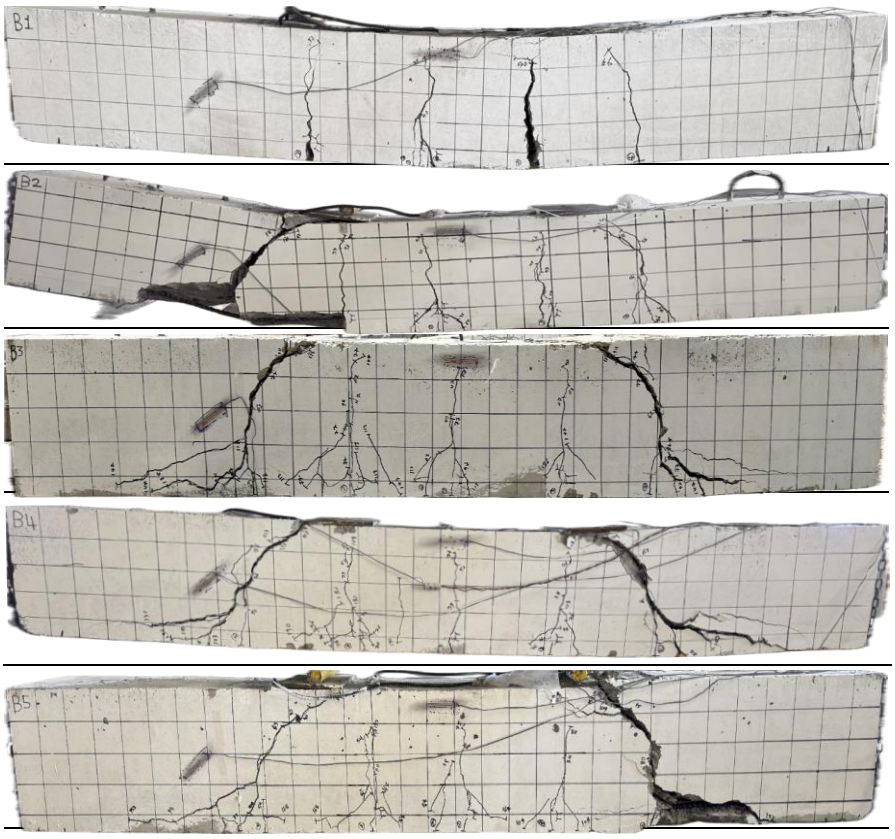


**Figure 9. Crack pattern**

Upon viewing Figures 10 to 14, the cracking history of the beams under gradual applied load is illustrated. This is the face of the beam where the randomly distributed speckle pattern is applied for DIC. The cracking load is determined from this analysis for more accuracy, as the strain is localized in the region of the crack before the crack is visible to the naked eye. This strain concentration is highlighted by color mapping (yellow to red), the load is recorded for the load cell reading, and the vertical mid-span displacement ($\Delta_Y$) and horizontal mid-span displacement ($\Delta_X$) are from DIC analysis. The differences in crack patterns are primarily influenced by the longitudinal reinforcement ratio ($\rho$), which increases progressively from Beam B1 to Beam B5. The progression in reinforcement ratio has a noticeable impact on the cracking behavior, ultimate load capacity, and failure mechanisms of the beams.

**Table 7. Failure mode and no. of cracks**

| Beam No. | No. of Cracks | Location | Failure Mode |
|---|---|---|---|
| B 1 | 4 (5)* | The first two cracks appeared at the bending span, the remaining under point load and one just outside point load. All cracks are straight, with no significant legs, and crack widths rapidly increase immediately after initiation. | Flexural |
| B 2 | 5 (8)* | Three vertical cracks at bending span, with an additional two each at the outside of a point load, beginning straight before concaving toward the point load.` | Flexural-Shear |
| B 3 | 5 (12)* | Three vertical cracks at the bending span, with noticeable legs, an additional two each at the outside of a point load sloped toward the supports, causing near-simultaneous failure in the two shear spans. | Flexural-Shear |
| B 4 | 6 (11)* | Four vertical cracks at bending span, with fewer legs than B3, with an additional two each at the outside of a point, the load increased in width to an end, sloping toward the supports. | Flexural-Shear |
| B 5 | 6 (12)* | Three vertical cracks at the bending span, with legs, an additional two each at the outside of a point load sloped toward the supports, and one crack increased in width more, causing failure. | Flexural-Shear |

* Number of cracks, including branches.

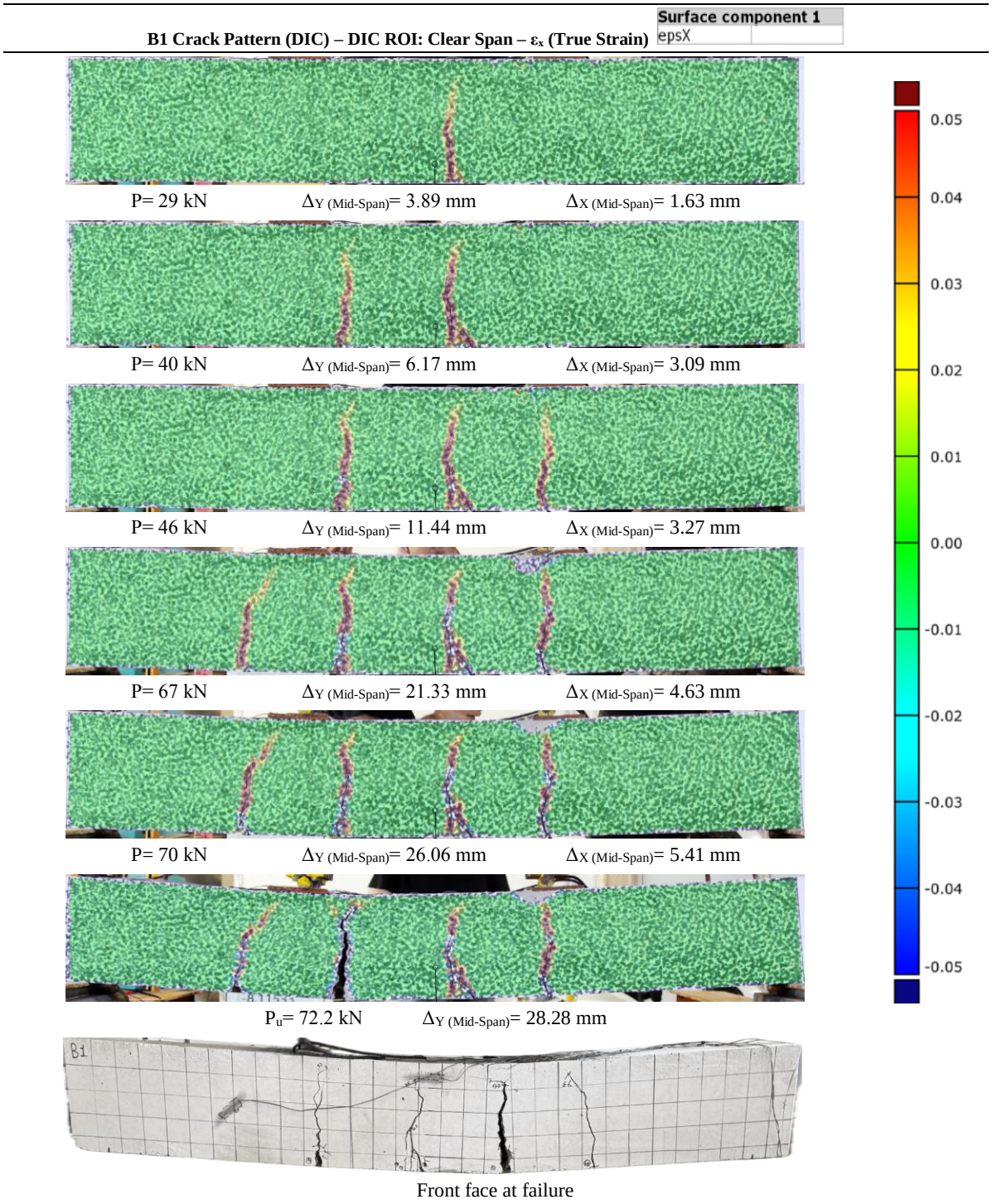


**Figure 10. B1 Cracking history**

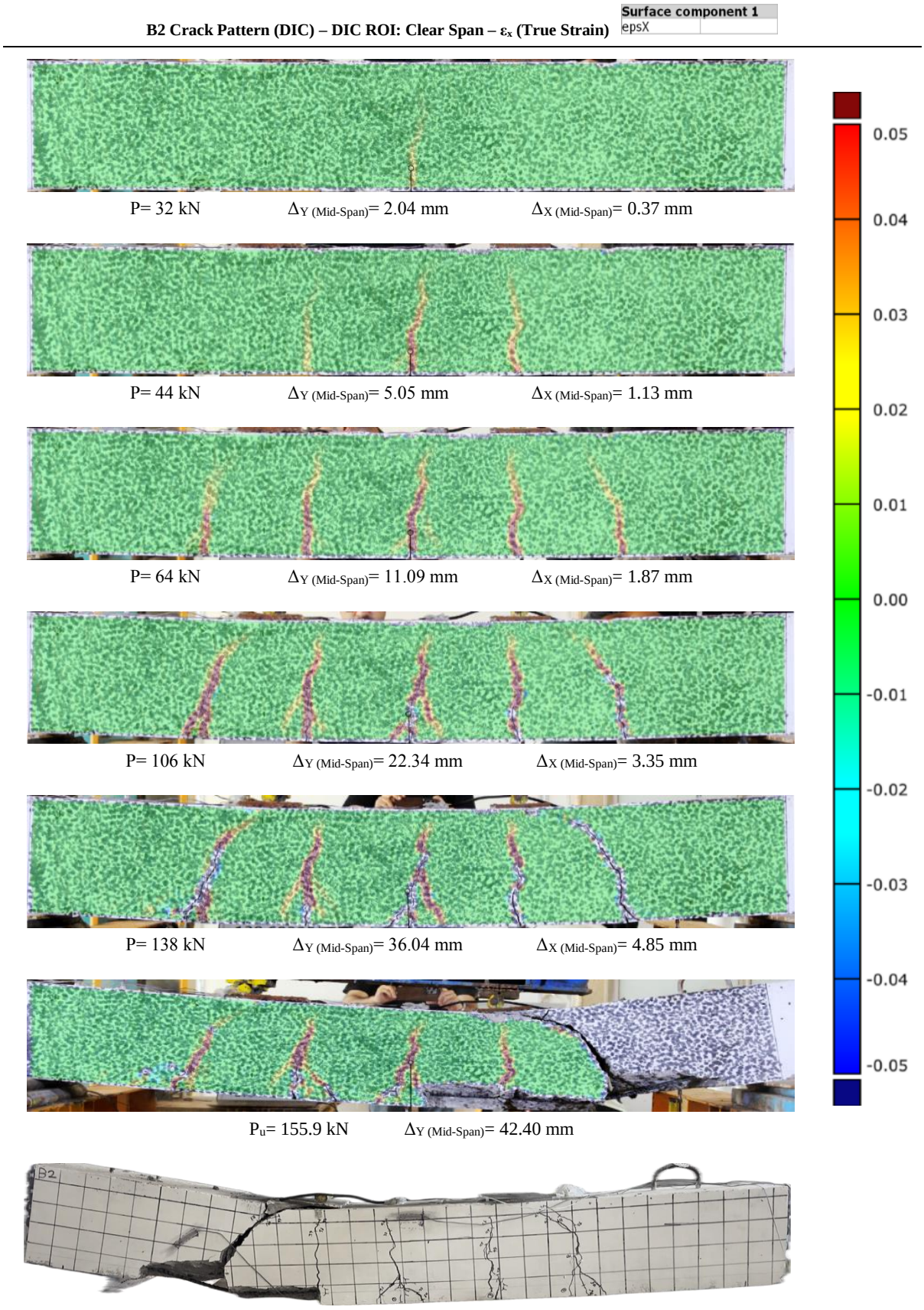


**Figure 11. B2 Cracking history**

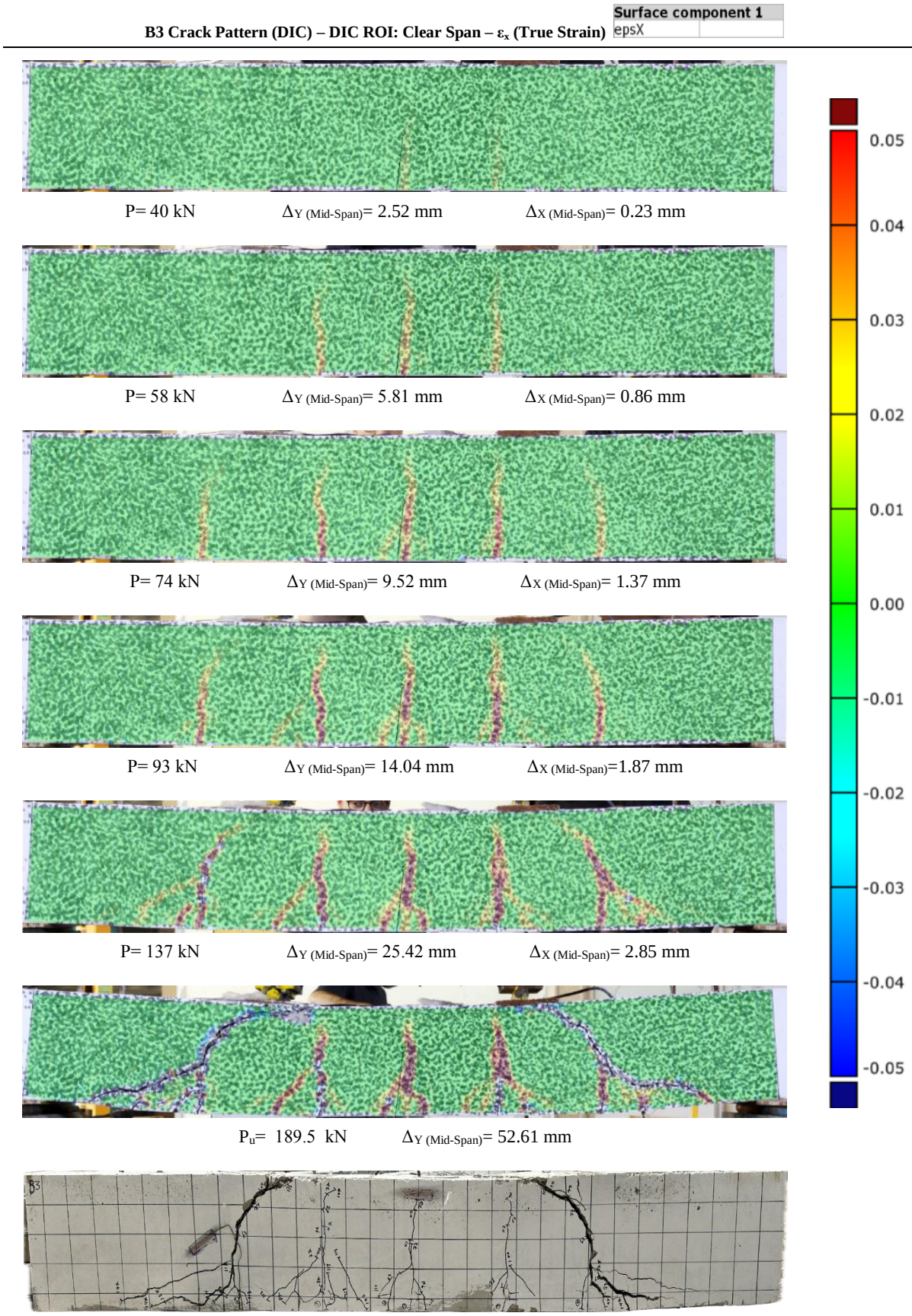


**Figure 12. B3 Cracking history**

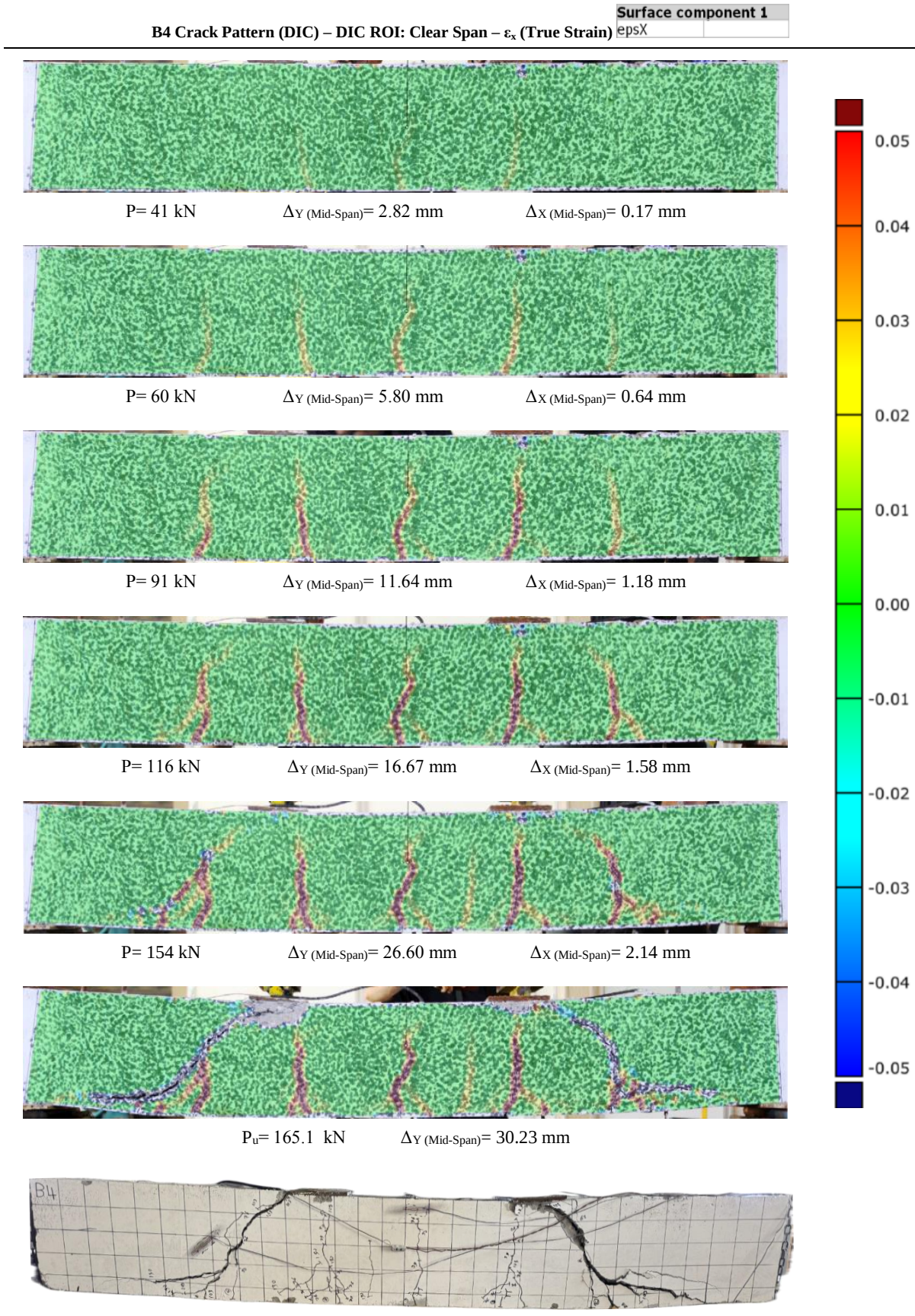


**Figure 13. B4 Cracking history**

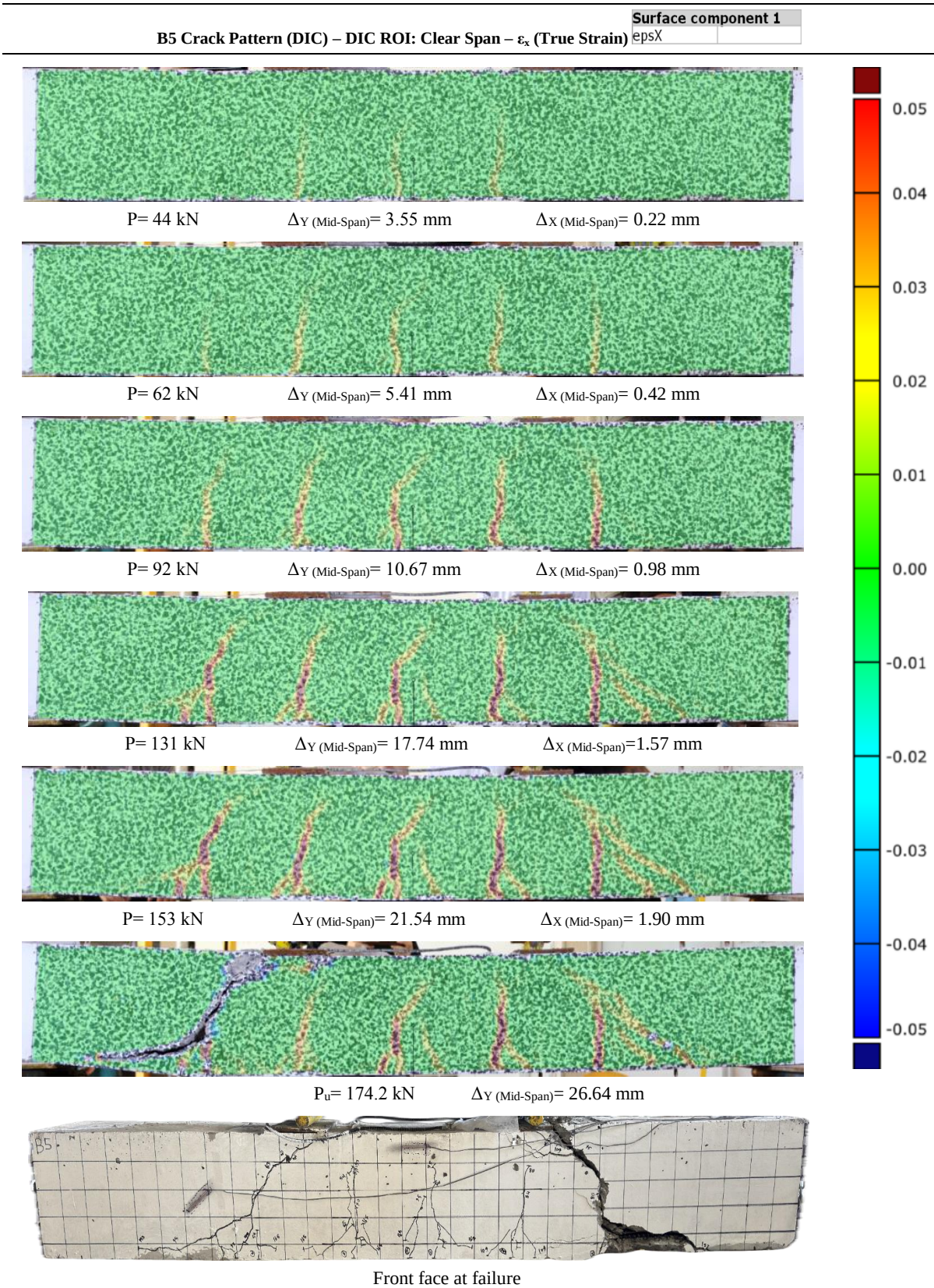


**Figure 14. Cracking history**

Beam B1, with the lowest reinforcement ratio (ρ = 0.47), exhibited cracks initiating at the lowest load, approximately 29 kN. These cracks propagated quickly across the span, forming fewer, wider cracks with minimal branching. Beam B2, with a higher reinforcement ratio (ρ = 0.9), improved crack control, with crack initiation occurring at a higher load of 32 kN. While the cracks were less wide than B1, they were still less distributed than beams with higher reinforcement ratios. Beam B3, with a 1.35 reinforcement ratio, marked a significant improvement in crack control. Cracks were initiated at a load of approximately 40 kN, and their propagation was more controlled. The cracks were denser, narrower,

and better distributed across the span. Similarly, Beam B4, with a reinforcement ratio of 1.8, further delayed crack initiation to 41 kN. The cracks in Beam B4 were finer, more closely spaced, and propagated in a more distributed pattern, reflecting enhanced tensile strain redistribution along the beam. B5, with the highest reinforcement ratio ($\rho = 2.25$), demonstrated the best cracking behavior performance. Crack initiation occurred at a higher load of 44 kN, and the crack distribution was the densest among the test beams. The progression of cracking was gradual, and the cracks showed significant branching and limited width, indicating superior stress redistribution.

The trend among the five beams highlights the significant influence of the reinforcement ratio on cracking behavior. As the reinforcement ratio increased from B1 to B5, the cracking load increased, and the cracks became more distributed. Beams with higher reinforcement ratios were better able to control crack width, leading to improved serviceability, and beams with lower reinforcement ratios showed brittle failure mechanisms, reflecting reduced performance. The longitudinal reinforcement ratio plays a critical role in the performance, and the crack control improved significantly with increased reinforcement. Beam B5, with the highest reinforcement ratio, showed the best overall performance, whereas Beam B1, with the lowest reinforcement ratio, exhibited the weakest performance. This trend underscores the importance of selecting an appropriate reinforcement ratio to achieve desirable cracking behavior and structural performance.

The cracking patterns observed in the beams indicate the interplay between flexural and shear stresses, with distinct differences based on the reinforcement ratios. Beams with lower reinforcement ratios exhibited fewer cracks, primarily concentrated in the bending span, whereas beams with higher reinforcement ratios showed more significant cracks distributed across the shear spans. The development of crack legs and the branching of cracks near the supports were more pronounced in beams with higher reinforcement, demonstrating their ability to sustain higher loads before failure. Additionally, Table 7 highlights the progression from flexural-dominated cracking in the early stages to flexural-shear failure at ultimate load, emphasizing the transition of the governing failure mode with increasing load.

The reinforcement ratio significantly affected the cracking behavior of concrete beams reinforced with GFRP. Increasing the reinforcement ratio resulted in a denser cracking pattern, which is due to the increased availability of reinforcement, which distributes stresses more evenly and prevents crack propagation across larger sections, as the greater reinforcement area provides better resistance to tensile stresses and delays the appearance of cracks, enhancing the beam's ability to withstand loads before cracking occurs and improving crack width control, resulting in more minor cracks even at higher load levels, enhancing serviceability by maintaining narrower cracks, which is essential for long-term durability and structural integrity. The lowest reinforcement ratio beam (B1) exhibited brittle failure after cracking, as GFRP lacks ductility. The limited reinforcement area could not redistribute stress effectively once cracking was initiated. This premature failure can be avoided with higher reinforcement ratio adoption, as the reinforcement ratio affects the load-carrying capacity and contributes to more controlled and gradual failure modes. Lower reinforcement ratio beams resulted in an earlier onset of fewer, widely spaced cracks formed at more significant intervals along the beam span. Each crack is then imposed to more strain and deformation. The reduced reinforcement fails to control crack opening effectively. The larger crack widths can impair serviceability and expose internal concrete and reinforcement to aggressive environmental conditions.

### 5.2.2. Crack Width

In lightly reinforced sections, crack width limitations are more restrictive than concrete stresses. However, concrete compressive stress becomes the governing factor in sections with higher reinforcement ratios [48]. As such, crack width measurements were taken at the side face of the beam and the bottom, using a crack width camera as illustrated in (Figure 15), which shows a crack width measurement of 1.30mm obtained using a crack monitoring device (HC-F600 by Hichance). The crack width progression of test beams at various load levels is examined in this section. Crack measurements were taken at three main points: mid-span, left of mid-span, and right of mid-span.

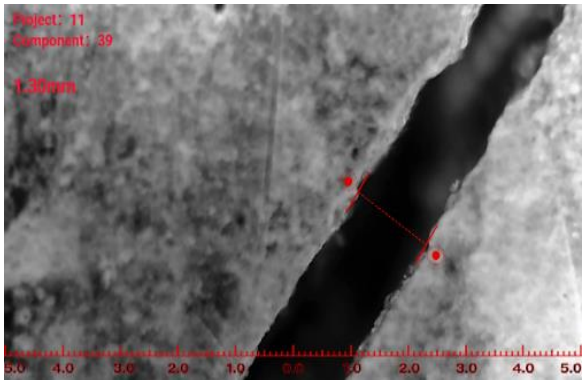


**Figure 15. Crack width measurement**

At lower reinforcement ratios (B1 and B2), crack widths increased more rapidly at lower loads, with B1 showing stable crack widths until higher loads, where cracks expand noticeably. For these beams, the rapid increase in crack width as loads rise suggests reduced stiffness and less control over crack propagation under service and ultimate loading conditions. Moderate reinforcement ratio B3, with a reinforcement ratio of 1.35, shows delayed crack initiation compared to B1 and B2. Initial cracks appear at moderate loads, with a less steep increase in crack width than in lower-reinforced beams, suggesting improved but limited crack control. At a specific load limit, the mid-span crack width in Beam B3 starts to settle, displaying negligible growth in mid-span crack width despite increasing stress. This behavior differs from the cracks on the left and right sides, which steadily expand under more significant stress. The stabilization at mid-span is probably caused by load redistribution, wherein augmented GFRP reinforcement improves crack bridging. The reinforcement at mid-span absorbs and distributes tensile forces more effectively after initial cracking, slowing further crack propagation. However, the left and right cracks from the mid-span experience more direct stress concentration without the same reinforcement effectiveness, leading to continued widening under load. Higher reinforcement ratios (B4 and B5) delay crack initiation and maintain narrower cracks across all load levels. The additional GFRP reinforcement enhances stiffness, limiting crack propagation under service and ultimate load conditions, providing better control over crack width, and improving durability.

For the mid-span crack shown in Figures 16 and 17, beams with lower reinforcement ratios (B1, B2) exhibited a rapid increase in crack width under load, suggesting less resistance to crack growth. B3 shows a moderate increase in crack width initially, but the mid-span crack width stabilizes after reaching a specific load, as explained above. B4 and B5, with higher reinforcement, demonstrate significantly narrower crack widths under equivalent loads, underscoring the reinforcement's effectiveness in crack control at mid-span.

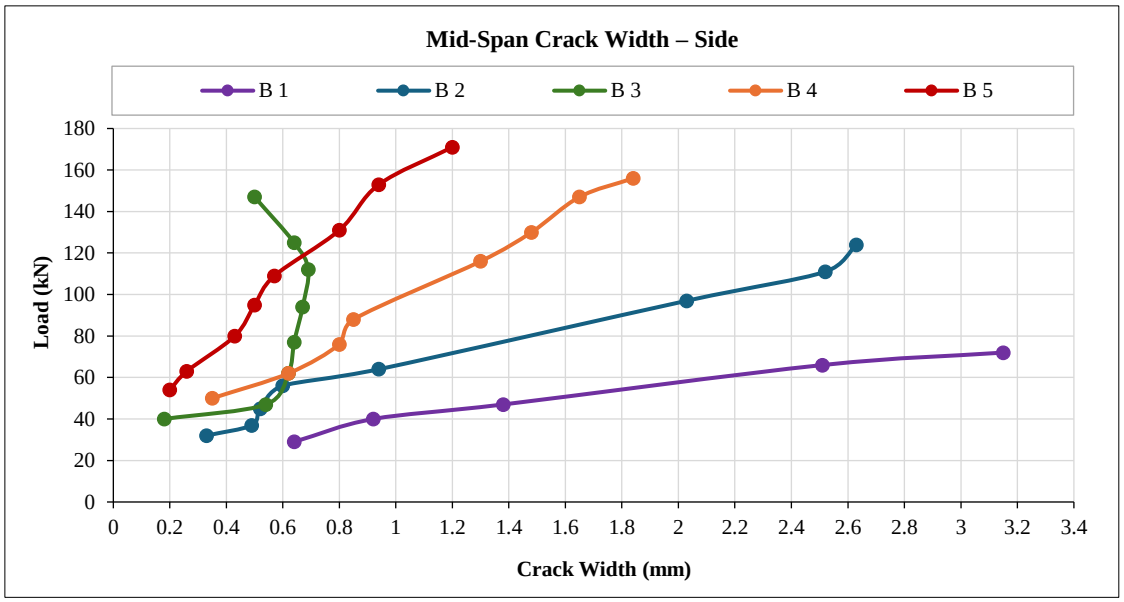


**Figure 16. Mid-span load-crack width (side)**

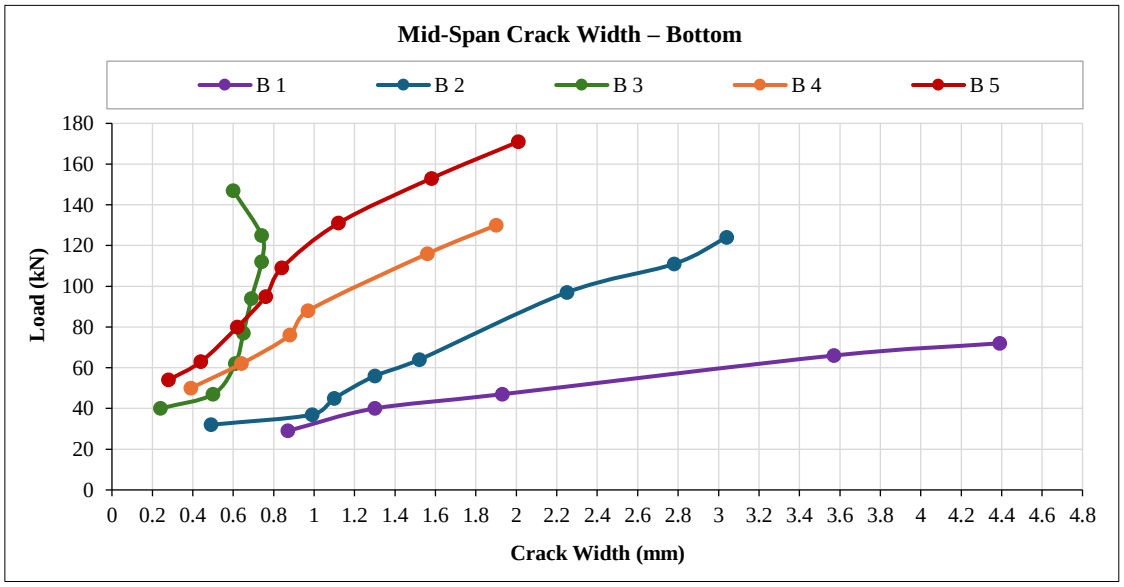


**Figure 17. Mid-span load-crack width (bottom)**

For sides cracks (Figures 18 and 19), higher-reinforced beams (B4, B5) consistently display narrower cracks across the load spectrum, while Beam B3 performs moderately in crack control, with narrower cracks than B1 and B2 but wider than B4 and B5. The mid-span crack stabilizes, and the left and right-side cracks continue widening, highlighting the localized effect of reinforcement in controlling crack growth at mid-span. All beams exhibit slight asymmetry in crack width between the left and right sides at mid-span. However, beams with higher reinforcement ratios (B4, B5) and moderate reinforcement (B3) display enhanced crack stability on both sides relative to lower-reinforced beams (B1, B2), suggesting that additional GFRP reinforcement restricts the influence of these asymmetries on the crack width.

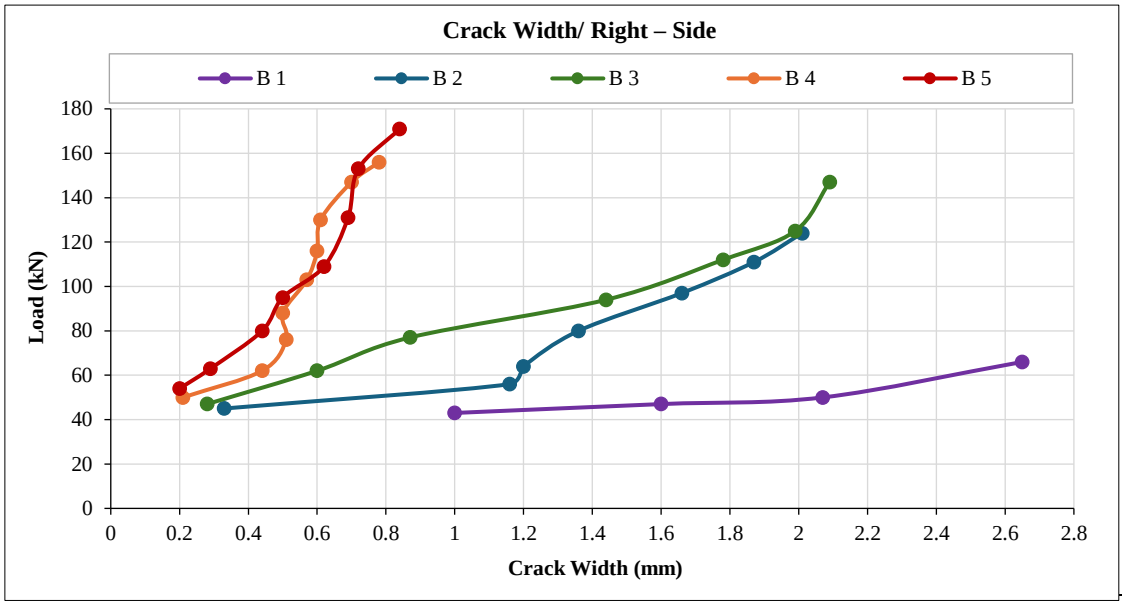


**Figure 18. Right load-crack width**

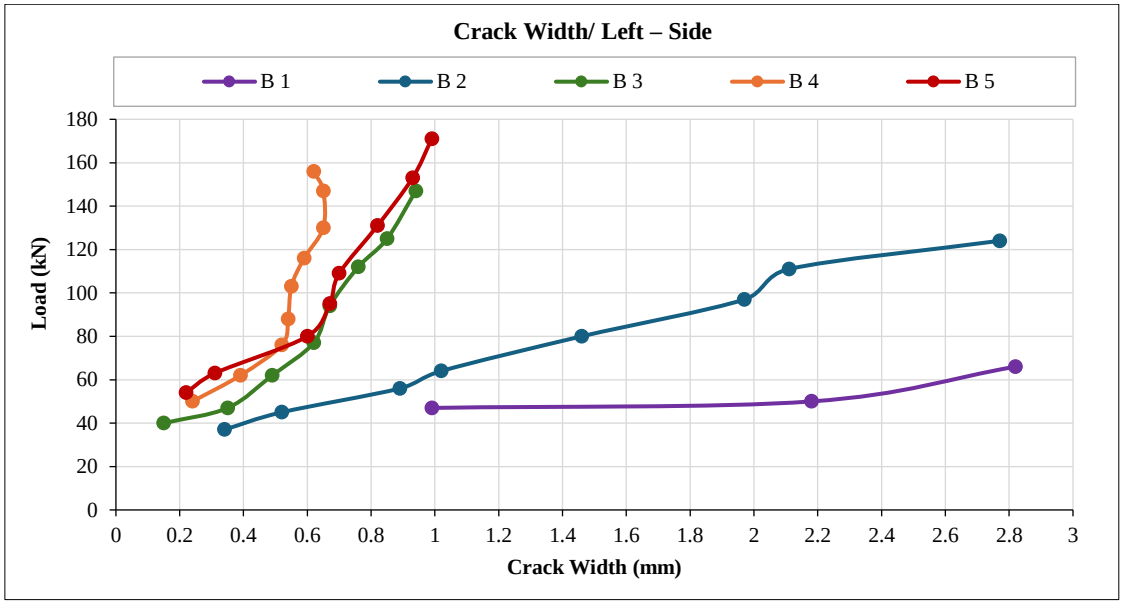


**Figure 19. Left load-crack width**

In contrast to steel, GFRP reinforcement does not exhibit yielding prior to failure, leading to a distinct crack-controlling mechanism. Higher-reinforced beams (B4 and B5) showed an extended elastic response, maintaining minor crack widths at increased loads. In beams with reduced reinforcement (B1, B2), cracks propagate more readily after initial cracking, resulting in accelerated widening. Beam B3 demonstrated a modest elastic response, with crack widening occurring later than in B4 and B5, but not to the same extent. Under service loads, the higher-reinforced beams (B4, B5) sustain crack widths below 1 mm, but B3 exhibits moderate crack widths, ranging from 0.5 mm to 1.5 mm, indicating satisfactory performance but restricted control over the long term. Lower-reinforced beams (B1, B2) surpass these widths more rapidly, suggesting potential serviceability concerns under further loads, with significant crack spreading, underlining the significance of increased reinforcement ratios for crack control (see Table 8).

**Table 8. Crack width observations**

| Beam No. | $\rho_f/\rho_{fb}$ | Crack Width Observations |
|---|---|---|
| B 1 | 0.5 | Experiences early cracking, rapid crack width growth, and substantial widening at higher loads, indicating that lower reinforcement ratios struggle to control cracks effectively. |
| B 2 | 0.9 | This beam shows a similar trend to B1, but with marginally improved crack control, crack widths are still significant at service and ultimate loads. |
| B 3 | 1.35 | It exhibits moderate crack control, and delays in initial crack width growth are observed, though ultimate load levels still present considerable widening. |
| B 4 | 1.8 | Shows enhanced crack control, with narrower crack widths at service and ultimate load levels compared to B1-B3. |
| B 5 | 2.25 | Demonstrates the best crack control, with delayed crack initiation and narrower crack widths maintained across all load levels, particularly at ultimate load. Underscoring the benefits of higher reinforcement ratios. |

### 5.2.3. Crack Spacing and Cracking Load

B5 has the most significant maximum crack spacing at 370 mm, significantly higher than the other beams, indicating wider spacing between cracks before failure. Also, the smallest minimum crack spacing at 195 mm indicates a more significant variability in crack spacing across this beam, with some areas experiencing tighter crack formation. The other beams have maximum crack spacing that is relatively close, ranging from 280 mm (B3) to 293 mm (B2 and B4), as shown in Table 9. B1 has the smallest maximum crack spacing (286 mm), suggesting it tends to crack more frequently across its length under loading, and shows minimum crack spacing ranging from 228 mm (B2) to 247 mm (B4), suggesting relatively consistent crack spacing within each beam. For the average crack spacing, B5 again has the most significant average crack spacing at 286 mm, and B1 has the smallest average crack spacing at 256 mm.

**Table 9. Crack spacing and cracking load**

| Beam No. | Cracks Spacing | | | Cracking Load | |
|---|---|---|---|---|---|
| | $S_{cr.,(Max)}$ (mm) | $S_{cr.,(Min)}$ (mm) | $S_{cr.,(avg)}$ (mm) | $P_{cr}$ (kN) | $\frac{P_{cr}}{P_u}$ % |
| B 1 | 286 | 234 | 256 | 29 | 40.2 |
| B 2 | 293 | 228 | 264 | 32 | 20.5 |
| B 3 | 280 | 234 | 257 | 40 | 21.1 |
| B 4 | 293 | 247 | 268 | 41 | 24.8 |
| B 5 | 370 | 195 | 286 | 44 | 25.3 |

The highest cracking load along the beams was of B5 at 44 kN, indicating it can withstand a higher load before the first crack forms. B4 follows with a cracking load of 41 kN. The mid-range cracking loads are observed in Beam B2 (32 kN) and Beam B3 (40 kN), while Beam B1 has the lowest cracking load at 29 kN with the highest Pcr/Pu percentage (40.2%), indicating that it cracks at a load that constitutes a large proportion of its ultimate load, which could suggest an early onset of cracking relative to its ultimate capacity. Beam B2 shows the lowest Pcr/Pu ratio (20.5%), representing that it reaches its first crack at a lower fraction of its ultimate load, suggesting potential early cracking behavior. Beams B3, B4, and B5 have moderate $P_{cr}/P_u$ percentages (21.1% to 25.3%), meaning they experience cracking at a moderate proportion of their load-bearing capacity. Beam B5 exhibits the highest cracking load (44 kN) and the broadest average crack spacing (286 mm), showing that its structural configuration or material properties allow it to withstand higher loads before cracking and form cracks generally spaced farther apart.

However, it has a relatively low $P_{cr}/P_u$ percentage (25.3%), implying that it cracks at a lower fraction of its ultimate load. Beams B2, B3, and B4 show moderate values for cracking load and crack spacing, representing intermediate behavior. Beam B2 has the lowest $P_{cr}/P_u$ ratio (20.5%), suggesting it may crack at a lower load relative to its capacity, while Beam B4 has a slightly higher cracking load (41 kN) and a moderate crack spacing distribution. Beam B1 has the smallest average crack spacing (256 mm) and the lowest cracking load (29 kN). Despite this, it has the highest $P_{cr}/P_u$ ratio (40.2%), indicating that cracks develop at a significant proportion of its ultimate capacity, which could imply that Beam B1, while prone to cracking at lower loads, distributes the cracking effect more densely across its length. The variability in crack spacing (both maximum and minimum) and cracking loads across the beams suggest that differences in reinforcement ratios significantly affect their crack formation and load-bearing capacity. Higher cracking loads with larger crack spacing (as seen in Beam B5) may indicate a design that prioritizes strength before cracking but sacrifices uniform crack distribution.

### 5.3. Strain

Higher reinforcement ratios improve capacity in the compression zone, with strains being more evenly distributed as the beams reach higher loads. Providing better resistance to flexural cracking and delays failure. For B3, B4, and B5, compression strains increase significantly as the reinforcement ratio increases consistently at failure load with reinforcement ratios up to 1.35, proposing a better distribution of internal forces and more effective use of concrete in compression. The compression strain increases. Lower reinforcement ratios result in higher stress and strain in the tension reinforcement, and B4 and B5 exhibit lower tension strains due to better stress distribution and reduced individual bar stress, as shown in Figures 20 and 21.

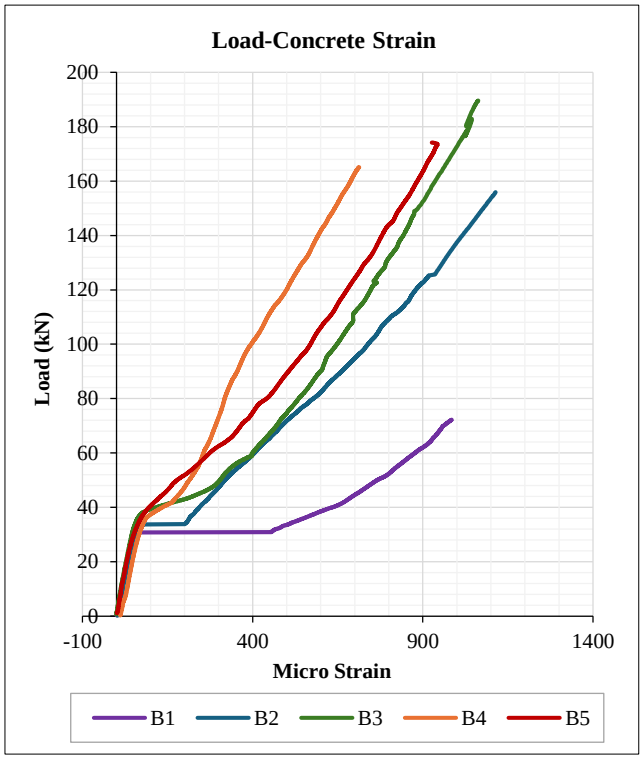


**Figure 20. Concrete strain**

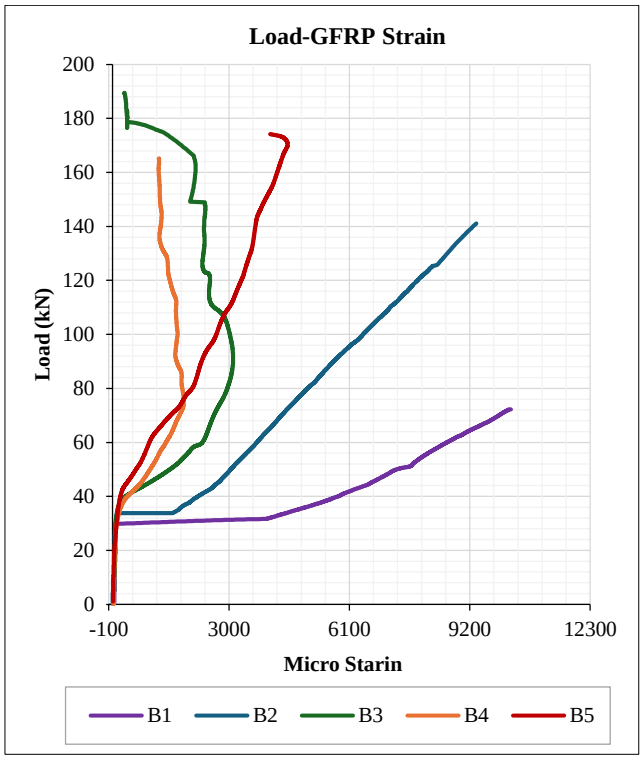


**Figure 21. GFRP strain**

## 5.4. Serviceability

The deflection and crack width govern the serviceability of concrete beams reinforced with GFRP bars. The American Concrete Institute's ACI 440.1R-15 [3] guideline commentary limits allowed crack widths for serviceability of 0.4mm and 0.7mm, contingent upon the structure's exposure circumstances. This divergence mainly arises from the durability specifications for the environment. The limitation is mostly for esthetic purposes since FRP is resistant to corrosion. For deflection, the service deflection limit is L/240. This ensures that excessive deflection does not compromise the usability or appearance of the structure. These factors ensure the beam performs adequately under service loads without compromising structural integrity or user comfort. Evaluating these parameters during design and analysis is critical, particularly for FRP-reinforced beams. FRP has a lower modulus of elasticity than steel, which can lead to more considerable deflections under load. Therefore, selecting reinforcement ratios and structural configurations is important to ensure compliance with serviceability requirements. The analysis showed (Table 10) that higher reinforcement ratios significantly increase the load required to produce a crack width of 0.4 mm, improving crack resistance (B5 with 2.25%, 76.5 kN). At a crack width of 0.7 mm, the load percentages for such cracks average around 43.6% of the ultimate load, although service loads constitute a more significant percentage, averaging 42.6% of the ultimate load. This emphasizes the impact of the reinforcement ratio on serviceability.

**Table 10. Service Loads**

| Beam No. | Cracking Load | | | | Service Load – Deflection | | |
|---|---|---|---|---|---|---|---|
| | $P_{Crack\ (kN)\ 0.4mm}$ | $\frac{P_{Crack\ 0.4}}{P_{Ultimate}}$ % | $P_{Crack\ (kN)\ 0.7mm}$ | $\frac{P_{Crack\ 0.7}}{P_{Ultimate}}$ % | $P_{Service\ (kN)}$ | $\frac{P_{Service}}{P_{Ultimate}}$ % | $\Delta_{Service\ \frac{L}{240}\ (mm)}$ |
| B1 | - | - | 25 | 34.6 | 40.8 | 56.5 | |
| B2 | 34 | 21.8 | 58.5 | 37.5 | 55.7 | 35.7 | |
| B3 | 43.5 | 22.9 | 68[R] | 35.9 | 66.7 | 35.2 | 7.5 |
| B4 | 52 | 31.5 | 67 | 40.6 | 69.7 | 42.2 | |
| B5 | 76.5 | 43.9 | 121 | 69.5 | 75.8 | 43.5 | |

* R: Right side crack

The cracking load ($P_{cr}$) represents the load at which the first visible crack appears in each beam, observed during loading and confirmed and adjusted from DIC analysis and longitudinal bars strain gages. Figure 22 demonstrating a steady increase in cracking loads with reinforcement ratio, peaking at B5 with 44 kN. Cracking loads increase progressively with higher reinforcement ratios. The increase in cracking load from B1 to B5 indicates a correlation between higher reinforcement ratios and delayed cracking. B3 and B4 show similar cracking loads, suggesting a plateau effect where additional reinforcement does not significantly impact early cracking behavior.

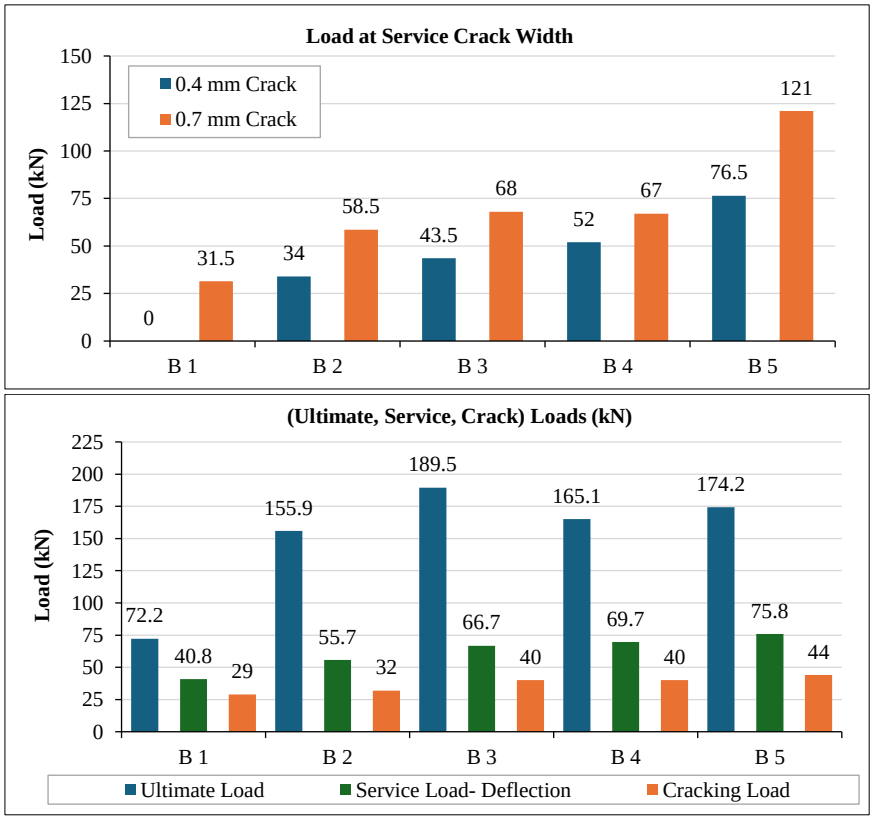


**Figure 22. Service loads**

## 5.5. Neutral Axis Depth

The neutral axis depth ($c$) measured from the compression zone in bending is relatively deep at low loads because both concrete in tension and reinforcement contribute to tensile resistance. As the applied load increases, cracks form in the tension zone, reducing its contribution to resisting the bending moment. Wider and closely spaced cracks in the tension zone cause a higher reduction of the effective tension zone, influencing the neutral axis depth and shifting it toward the compression zone due to the nonlinearity of concrete stress distribution and the progressive cracking in the tension zone, indicating the need to preserve a balance between the compressive and tensile forces inside the cross-section. At the ultimate load, the natural axis (NA) stabilizes close to the compression zone. This position indicates potential concrete crushing for over-reinforced sections, whereas the shift reflects the tensile reinforcement yield before concrete failure for under-reinforced sections. Diagonal shear and flexural cracks influence stress distribution, causing a significant neutral axis shift. Diagonal tension forces in the shear span cause additional compression in the concrete due to shear, leading to a shallower NA. At the flexure region, the NA is deeper because of compression and tension caused by bending. The relation between the strain in the tension bars and the strain of the concrete compression fiber based on the assumption of a linear strain distribution across the cross-section:

$$\frac{\varepsilon_c}{c} = \frac{\varepsilon_t}{d-c} \quad \text{Rearranging for c} \rightarrow \quad c = \left(\frac{\varepsilon_{cu}}{\varepsilon_{cu}+\varepsilon_{fu}}\right) d \qquad \text{(ACI 440.1R-15) [3]} \qquad (6)$$

At ultimate load, the neutral axis depth for B1 is 22.8 mm, showing the shallowest neutral axis depth among all beams. This is attributed to its low reinforcement ratio and limited reinforcement tensile capacity. Beams B2 and B3 demonstrate significantly deeper neutral axis depths (233.3 mm and 202.7 mm, respectively), highlighting the contribution of higher reinforcement ratios to mobilizing the concrete compression zone. However, B4 and B5 exhibit a decrease in the neutral axis to 97.4 mm and 48.3 mm, respectively, despite their higher reinforcement ratios. GFRP reinforcement is brittle and fails at ultimate tensile strength. For beams with higher reinforcement ratios, the failure may occur before fully mobilizing the compression zone, leading to a shallower neutral axis depth. Higher reinforcement ratios increase stiffness, reducing the strain in the compression zone and limiting the neutral axis depth under load. In stiffer sections (B4 and B5), the balance of forces may shift earlier, resulting in a reduced compression zone and a shallower neutral axis depth, likely due to the rapture of tension reinforcement before the concrete can fully utilize the compression forces (Table 11).

**Table 11. Neutral axis depth**

| Beam No. | $P_{crack}$ | | | $P_{service}$ | | | $P_{ultimate}$ | | |
|---|---|---|---|---|---|---|---|---|---|
| | $\varepsilon_c$ ($10^6$) | $\varepsilon_t$ ($10^6$) | c (mm) | $\varepsilon_c$ ($10^6$) | $\varepsilon_t$ ($10^6$) | c (mm) | $\varepsilon_c$ ($10^6$) | $\varepsilon_t$ ($10^6$) | c (mm) |
| B1 | 53.4 | 83 | 102.4 | 7038 | 52.1 | 22.1 | 984.4 | 10242.9 | 22.8 |
| B2 | 65.8 | 91.6 | 108.7 | 366.9 | 3427.2 | 25.1 | 1113.0 | 9369.2 | 233.3 |
| B3 | 115.3 | 338.6 | 66.0 | 447.1 | 2515.8 | 39.23 | 1062.4 | 300.6 | 202.7 |
| B4 | 134.6 | 385.5 | 67.3 | 289.5 | 1710.1 | 37.6 | 713.2 | 1190.6 | 97.4 |
| B5 | 129.4 | 313.6 | 75.9 | 404.9 | 1823.1 | 47.4 | 926.4 | 4062.2 | 48.3 |

## 5.6. Ductility Index

The capacity to undergo significant plastic deformation before failure, allowing for energy dissipation and providing warning signs before collapse, is crucial for preventing sudden failure, especially in seismic regions, as it enables structures to absorb and dissipate energy. GFRP-reinforced concrete beams exhibit different ductility characteristics compared to steel-reinforced beams. Unlike steel, GFRP lacks a distinct yield point and behaves linearly until failure, leading to a more brittle failure mode with limited plastic deformation. This reduced ductility presents challenges in design, which is addressed by the ACI 440 by designing beams to be over-reinforced to ensure adequate warning before failure. Ductility is assessed in steel reinforced beams using the deflection or curvature ductility index, the ratio of ultimate load to yield load. Without a clear yield point, 0.65 of the ultimate load is used as an alternative to the yield point for ductility evaluation.

$$\text{Ductility Index} = \frac{\Delta_{@Pu}}{\Delta_{@0.65Pu}} \qquad (7)$$

The ductility indices range from 1.8 to 2.49 among the testing beams, as shown in Table 12, with B1 having the highest ductility index of 2.49, likely because it has the lowest reinforcement ratio, allowing for more deformation before failure. Moreover, B3 showed a comparable ductility index of 2.45. The ductility index values decrease as the reinforcement ratio increases. While higher reinforcement ratios (B4 and B5) result in more brittle behavior, likely because the beams become more rigid with increased reinforcement, aligning with the behavior of GFRP-reinforced

concrete beams, as GFRP lacks yielding behavior, B3 avoids this issue. It may be due to a synergy between the longitudinal GFRP bars and stirrup spacing, which helps resist flexure and shear. The ultimate deflection (Δu) is highest for B3 (52.6 mm), which correlates with its greatest load-carrying capacity among all beams ($P_u$ = 189.5 kN), reflecting a good balance between strength and deformability. This is noteworthy given that higher reinforcement ratios typically result in reduced ductility, yet Beam B3 still exhibits a favorable ductility index.

**Table 12. Ductility indices**

| Beam No. | Pu | Δu | 0.65$P_u$ | Δ @0.65$P_u$ | Ductility Index |
|---|---|---|---|---|---|
| B 1 | 72.2 | 28.3 | 46.9 | 11.3 | 2.49 |
| B 2 | 155.9 | 42.4 | 101.3 | 20.9 | 2.02 |
| B 3 | 189.5 | 52.6 | 123.2 | 21.5 | 2.45 |
| B 4 | 165.1 | 30.2 | 107.3 | 15.1 | 2.01 |
| B 5 | 174.2 | 26.6 | 113.2 | 14.8 | 1.80 |

The observed failure modes of B4 and B5 were primarily shear-dominated with limited signs of ductility before failure. Significant diagonal shear cracks developed before failure in both cases, particularly in the shear span. Failure occurred suddenly, with a rapid loss of load-carrying capacity once the critical shear crack propagated. Beam B5 (highest reinforcement ratio, ρ = 2.25%) exhibited the most brittle behavior, with minimal pre-failure deformation and an abrupt failure mechanism. Beam B4 (ρ = 1.8%) showed slightly more deformation before failure but still exhibited a shear-dominated failure mode. Despite the high reinforcement ratios, no yielding or strain softening was observed in the GFRP reinforcement, confirming that failure was governed by shear capacity limitations rather than flexural ductility. The absence of a yielding phase in GFRP reinforcement contributed to the brittle nature of failure. While some pre-failure crack development was observed, particularly in the tension zone, the overall response of B4 and B5 aligns with the expected behavior for highly reinforced GFRP beams in shear-dominated failure modes.

## 5.7. Ultimate Load Capacity

The calculation of the ultimate load due to shear and flexure per ACI Code-440.11-22 [31] and ACI 440.1R-15 [3] is presented in Table 13. The experimental load is slightly lower than the theoretical, likely due to material imperfections or assumptions in the theoretical model. The B1 ratio is 82.3% and 96.4% for B2, which closely approaches the theoretical prediction, showing good agreement and validating the design approach. B3 92.7% also strongly aligns with the theoretical predictions, supporting the accuracy. The gap between experimental and theoretical loads extends for higher reinforcement ratios, as B4 and B5 are 71.5% and 68.9%, respectively, highlighting potential challenges with using higher GFRP reinforcement ratios, which may indicate a reduced bond performance or brittle behavior which agree with previous research on GFRP-reinforced concrete beams, which indicate that increasing the reinforcement ratio enhances stiffness and serviceability but does not always lead to higher ultimate load capacity and may reduce capacity, suggesting a bond-slip and shear failure issues for shear-dominated failure beams. This highlights the need for further investigation into the role of bond-slip behavior and reinforcement distribution in high-reinforcement-ratio GFRP beams. Tu et al. (2022) [49] research indicates that exceeding a reinforcement ratio of 1.51 reduces the load-carrying capacity and does not result in a proportional increase. Kaszubska et al. (2017) [18] observed that increasing the reinforcement ratio of 1.35 to 1.8 of the same diameter bars had little effect on ultimate load capacity, especially in single-layer reinforcement configurations.

**Table 13. Experimental to theoretical $P_u$ ratio**

| Beam No. | Transverse Reinforcement | | Longitudinal Reinforcement | | | Theoretical $P_u$ (KN) | | Experimental $P_u$ (KN) | $\frac{P_{u,\ Exp.}}{P_{u,\ Theo.}}$ % |
|---|---|---|---|---|---|---|---|---|---|
| | $Ø_{st}$ (mm) | S (mm) | $Ø_{ba}$ (mm) | No. bars | $\rho_f/\rho_{fb}$ | $P_u$ shear | $P_u$ flexure | | |
| B 1 | 8 (GFRP) | 240 | 8 | 2 | 0.47 | 108.5 | 87.7 | 72.2 | 82.3 |
| B 2 | | | 12 | 2 | 0.9 | 108.2 | 161.8 | 155.9 | 96.4 |
| B 3 | | | | 3 | 1.35 | 108.2 | 204.0 | 189.5 | 92.7 |
| B 4 | | | | 4 | 1.8 | 108.2 | 230.8 | 165.1 | 71.5 |
| B 5 | | | | 5 | 2.25 | 108.2 | 253.0 | 174.2 | 68.9 |

## 6. Conclusions

- Higher reinforcement ratio beams showed enhanced stiffness and reduced deflection at service and ultimate load levels. B3 (ρ= 1.35) achieved the highest ultimate load capacity of 189.5 kN with a mid-span deflection of 52.6 mm, reflecting a balance between strength and deformability. In contrast, B1 (ρ= 0.5) showed the lowest ultimate load of 72.2 kN and a brittle failure mode. B5 (ρ= 2.25) demonstrated exceptional stiffness, with a deflection of only 26.6 mm at ultimate load, showcasing the potential of high reinforcement ratios in minimizing deformations.
- Crack propagation and crack spacing depended significantly on the reinforcement ratio. Cracking loads increased with higher reinforcement ratios, delaying the beginning of cracks. B5 delayed crack initiation to 44 kN and maintained average crack widths below 1 mm under service loads. B1 exhibited the earliest crack initiation at 29 kN and the widest cracks, highlighting the limitations of low reinforcement ratios. B3 achieved an optimal balance, with moderate crack widths and delayed crack initiation at 40 kN. Average crack spacing ranged from 256 mm (B1) to 286 mm (B5), demonstrating the effect of reinforcement ratios on crack distribution.
- The ductility index varied with reinforcement ratios, emphasizing the trade-off between stiffness and deformability. B3 achieved a favorable ductility index of 2.45, balancing strength and deformation, while B1 exhibited the highest index of 2.49 due to its lower stiffness. B5 had the lowest ductility index of 1.8.
- Higher reinforcement ratios generally deepen the neutral axis, except for B4 and B5, with reinforcement ratios of 1.8 and 2.25, respectively, where increased stiffness and brittle GFRP failure lead to shallower depths, limiting compression zone mobilization.
- Higher reinforcement ratios distribute strain more evenly and improve flexural cracking resistance, reducing tension strains due to better stress distribution.
- Theoretical predictions of $P_u$ aligned closely with experimental results for intermediate reinforcement ratios. B3 achieved 92.7% of its theoretical load capacity, validating its efficient design. In contrast, higher reinforcement ratios, such as in B5, showed divergences, achieving only 68.9% of the theoretical capacity due to bond limitations and brittle behavior.
- B4 and B5, with higher reinforcement ratios (1.8 and 2.25), demonstrate the best serviceability among the tested beams in terms of crack control, reduced crack widths, delayed crack initiation, and reduced crack widths under both service and ultimate loads with higher stiffness. B5 exhibited narrow cracks and minor deflection under service loads. B3 with (ρ= 1.35) demonstrated excellent serviceability, while lower reinforcement ratio beams showed excessive deflection and significant crack widths, compromising its performance.

The results underline the critical role of reinforcement ratios in optimizing the performance of GFRP-reinforced beams. Higher reinforcement ratios enhance strength, stiffness, and crack control. Raising the GFRP longitudinal reinforcement ratio to 1.35 enhanced load-carrying capacity performance. The capacity declined at higher reinforcement ratios (1.8, 2.25) while performing better in service crack widths and deflection, which may be due to a limit of bonding with concrete, as suggested by the horizontal cracks of B4 and B5. A 1.35 reinforcement ratio consistently emerged as the optimal configuration, achieving the best balance of strength, ductility, and serviceability.

## 7. Nomenclature

| | | | |
|---|---|---|---|
| $w/c$ | Water-Cement ratio | RC | Reinforced Concrete |
| $a/d$ | Shear span-to-depth ratio | FRP | Fiber Reinforced Polymer |
| $\rho_{fb}$ | Balanced Reinforcement Ratio | GFRP | Glass Fiber-Reinforced Polymer |
| $\rho_f$ | Reinforcement Ratio | CFRP | Carbon Fiber-Reinforced Polymer |
| Ø | Diameter of Bar | LVDT | Linear Variable Differential Transformer |
| $P$ | Applied Load | ACI | American Concrete Institute |
| $A$ | Cross-Sectional Area | ASTM | American Society for Testing and Materials |
| $d$ | Effective Depth | DAQ | Data Acquisition System |
| $\sigma$ | Stress | LVDT | Linear Variable Displacement Transformers |
| $\epsilon$ | Strain | DIC | Digital Image Correlation |
| $f'_c$ | Cylinder Compressive Strength of Concrete | RMC | Ready-Mix Concrete |
| $f_{cu}$ | Cube Compressive Strength of Concrete | BS EN | British Standard European Norm |
| $f_t$ $(T)$ | Splitting Tensile Strength | CEM | Cement |
| $f_r$ $(f_{cf})$ | Modulus of Rupture | | |
| $E_c$ | Modulus of Elasticity | | |

# 8. Declarations

## 8.1. Author Contributions

Conceptualization, A.I.S. and T.M.H.; methodology, A.I.S. and T.M.H.; software, T.M.H.; validation, A.I.S. and T.M.H.; formal analysis, T.H.M.; investigation, T.M.H.; resources, T.M.H.; data curation, T.M.H.; writing—original draft preparation, T.M.H.; writing—review and editing, A.I.S.; visualization, T.M.H.; supervision, A.I.S.; project administration, A.I.S.; funding acquisition, T.M.H. All authors have read and agreed to the published version of the manuscript.

## 8.2. Data Availability Statement

The data presented in this study are available in the article.

## 8.3. Funding

The authors received no financial support for the research, authorship, and/or publication of this article.

## 8.4. Conflicts of Interest

The authors declare no conflict of interest.

# 9. References

[1] Benmokrane, B., Wang, P., Ton-That, T. M., Rahman, H., & Robert, J.-F. (2002). Durability of Glass Fiber-Reinforced Polymer Reinforcing Bars in Concrete Environment. Journal of Composites for Construction, 6(3), 143–153. doi:10.1061/(asce)1090-0268(2002)6:3(143).

[2] Mohammed, S. A., & Said, A. M. I. (2024). Concrete beams reinforced with longitudinal and transverse GFRP bars. Magazine of Civil Engineering, 17(5), 1-4. doi:10.34910/MCE.129.8.

[3] ACI 440.1R-15. (2015). Guide for the Design and Construction of Concrete Reinforced with FRP Bars. American Concrete Institute (ACI), Michigan, United States.

[4] Kodsy, A. (2019). Bond Performance of Sanded Surface and Threaded Smooth GFRP Bars. Civil Engineering Research Journal, 8(4). doi:10.19080/cerj.2019.08.555743.

[5] Said, A. M. I., Hilfi, H. A., Allawi, A. A., & Wardeh, G. (2024). Structural Performance of a Hollow-Core Square Concrete Column Longitudinally Reinforced with GFRP Bars under Concentric Load. CivilEng, 5(4), 928–948. doi:10.3390/civileng5040047.

[6] Hussein, H. A., & Said, A. M. I. (2023). Finite Element Analysis of Axially Loaded GFRP-Reinforced Concrete Hollow Square Columns. E3S Web of Conferences, 427, 2023. doi:10.1051/e3sconf/202342702023.

[7] Nassif, N., Talha Junaid, M., Maalej, M., Altoubat, S., & Barakat, S. A. (2024). Durability of Fiber-Reinforced Polymer (FRP) Bars: Progress, Innovations and Challenges Based on Bibliometric Analysis. Civil Engineering Journal (Iran), 10, 136–173. doi:10.28991/CEJ-SP2024-010-09.

[8] Hussein, H. A., & Said, A. I. (2024). Experimental Investigation of GFRP-Reinforced Hollow Square Concrete Column. Journal of Engineering, 30(06), 108–124. doi:10.31026/j.eng.2024.06.07.

[9] Golham, M. A., & Al-Ahmed, A. H. A. (2024). Strengthening of GFRP Reinforced Concrete Slabs with Openings. Journal of Engineering, 30(01), 157–172. doi:10.31026/j.eng.2024.01.10.

[10] Ibrahim, T. H., & Allawi, A. A. (2023). The Response of Reinforced Concrete Composite Beams Reinforced with Pultruded GFRP to Repeated Loads. Journal of Engineering, 29(1), 158–174. doi:10.31026/j.eng.2023.01.10.

[11] Wegian, F. M., & Abdalla, H. A. (2005). Shear capacity of concrete beams reinforced with fiber reinforced polymers. Composite Structures, 71(1), 130–138. doi:10.1016/j.compstruct.2004.10.001.

[12] Ashour, A. F. (2006). Flexural and shear capacities of concrete beams reinforced with GFRP bars. Construction and Building Materials, 20(10), 1005–1015. doi:10.1016/j.conbuildmat.2005.06.023.

[13] Tavares, D. H., Giongo, J. S., & Paultre, P. (2008). Behavior of reinforced concrete beams reinforced with GFRP bars. Revista IBRACON de Estruturas e Materiais, 1(3), 285–295. doi:10.1590/s1983-41952008000300004.

[14] Nguyen-Minh, L., & Rovňák, M. (2011). Shear resistance of GFRP-reinforced concrete beams. Magazine of Concrete Research, 63(3), 215–233. doi:10.1680/macr.9.00182.

[15] Kalpana, V. G., & Subramanian, K. (2011). Behavior of concrete beams reinforced with GFRP BARS. Journal of Reinforced Plastics and Composites, 30(23), 1915–1922. doi:10.1177/0731684411431119.

[16] Maranan, G. B., Manalo, A. C., Karunasena, W. M., Benmokrane, B., & Mendis, P. A. (2015). Comparison of the shear behaviour of geopolymer concrete beams with GFRP and steel transverse reinforcements. Proceedings, Joint Conference of the 12th International Symposium on Fiber Reinforced Polymers for Reinforced Concrete Structures (FRPRCS-12) & the 5th Asia-Pacific Conference on Fiber Reinforced Polymers in Structures (APFIS-2015), 14-16 December, Nanjing, China.

[17] Said, M., Adam, M. A., Mahmoud, A. A., & Shanour, A. S. (2016). Experimental and analytical shear evaluation of concrete beams reinforced with glass fiber reinforced polymers bars. Construction and Building Materials, 102, 574–591. doi:10.1016/j.conbuildmat.2015.10.185.

[18] Kaszubska, M., Kotynia, R., & Barros, J. A. O. (2017). Influence of Longitudinal GFRP Reinforcement Ratio on Shear Capacity of Concrete Beams without Stirrups. Procedia Engineering, 193, 361–368. doi:10.1016/j.proeng.2017.06.225.

[19] Krasniqi, C., Kabashi, N., Krasniqi, E., & Kaqi, V. (2018). Comparison of the behavior of GFRP reinforced concrete beams with conventional steel bars. Pollack Periodica, 13(3), 141–150. doi:10.1556/606.2018.13.3.14.

[20] Menam, A., Kumar, K. S., & Rupa, P. (2021). Flexural and Shear Behavior of Beams Reinforced with GFRP Rebars. International Journal of Recent Technology and Engineering (IJRTE), 9(5), 229–235. doi:10.35940/ijrte.e5191.019521.

[21] Moawad, M. S., & Fawzi, A. (2021). Performance of concrete beams partially/fully reinforced with glass fiber polymer bars. Journal of Engineering and Applied Science, 68(1), 38. doi:10.1186/s44147-021-00028-6.

[22] Yuan, Y., Wang, Z., & Wang, D. (2022). Shear behavior of concrete beams reinforced with closed-type winding glass fiber-reinforced polymer stirrups. Advances in Structural Engineering, 25(12), 2577–2589. doi:10.1177/13694332221104280.

[23] Ali, H. H., & Said, A. I. (2023). Experimental Study on the Performance of Concrete Beams Including Holes Reinforced with Glass Fiber Polymer. E3S Web of Conferences, 427. doi:10.1051/e3sconf/202342702010.

[24] Ali, H. H., & Said, A. M. I. (2022). Flexural behavior of concrete beams with horizontal and vertical openings reinforced by glass-fiber-reinforced polymer (GFRP) bars. Journal of the Mechanical Behavior of Materials, 31(1), 407–415. doi:10.1515/jmbm-2022-0045.

[25] Abdulmuttalib Issa, M. A., Allawi, A. A., & Oukaili, N. (2024). Effects of GFRP Stirrup Spacing on the Behavior of Doubly GFRP-Reinforced Concrete Beams. Civil Engineering Journal (Iran), 10(2), 502–520. doi:10.28991/CEJ-2024-010-02-011.

[26] Abdulmuttalib Issa, M., Allawi, A. A., & Oukaili, N. (2024). Performance of doubly reinforced concrete beams with GFRP bars. Journal of the Mechanical Behavior of Materials, 33(1), 20220308. doi:10.1515/jmbm-2022-0308.

[27] Mohammed, S. A., & Said, A. I. (2024). A Comparative Study of the Structural Behavior of Concrete Beams Reinforced with Different Configurations of GFRP and Steel Bars. Journal of Engineering, 30(4), 200–218. doi:10.31026/j.eng.2024.04.12.

[28] Mohammed, S. A., & Said, A. M. I. (2022). Analysis of concrete beams reinforced by GFRP bars with varying parameters. Journal of the Mechanical Behavior of Materials, 31(1), 767–774. doi:10.1515/jmbm-2022-0068.

[29] Rasheed, M. R., & Mohammed, S. D. (2024). Structural behavior of one-way slabs reinforced by a combination of GFRP and steel bars: An experimental and numerical investigation. Journal of the Mechanical Behavior of Materials, 33(1), 1–22. doi:10.1515/jmbm-2024-0002.

[30] Zhao, J., Bao, X., Yang, S., Wang, Z., He, H., & Xu, X. (2024). Experimental and Theoretical Studies on the Shear Performance of Concrete Beams Reinforced with Fiber-Reinforced Polymer Stirrups. Materials, 17(3), 593. doi:10.3390/ma17030593.

[31] ACI 440.11-22. (2023). Building Code Requirements for Structural Concrete Reinforced with Glass Fiber-Reinforced Polymer (GFRP) Bars. American Concrete Institute (ACI), Michigan, United States.

[32] ACI 318-19. (2019). Building Code Requirements for Structural Concrete. American Concrete Institute (ACI), Michigan, United States.

[33] Reu, P. (2014). All about speckles: Speckle size measurement. Experimental Techniques, 38(6), 1–2. doi:10.1111/ext.12110.

[34] Jones, E. M. C., & Iadicola, M. A. (2018). A Good Practices Guide for Digital Image Correlation. International Digital Image Correlation Society, iDICs. doi:10.32720/idics/gpg.ed1.

[35] Said, A. I., & Tuma, N. H. (2021). Numerical Modeling for Flexural Behavior of UHPC Beams Reinforced with Steel and Sand-Coated CFRP Bars. IOP Conference Series: Earth and Environmental Science, 856(1), 12003. doi:10.1088/1755-1315/856/1/012003.

[36] Said, A. M. I., & Abbas, O. M. (2015). Evaluation of deflection in high strength concrete (HSC) I-beam reinforced with carbon fiber reinforced polymer (CFRP) bars. The 7th Asia Pacific Young Researchers and Graduates Symposium, 20-21 August, Kuala Lumpur, Malaysia.

[37] BS EN 197-1:2011. (2011). Cement – Composition, Specifications and Conformity Criteria for Common Cements. British Standard (BSI), London, United Kingdom.

[38] ASTM C33/C33M-18. (2023). Standard Specification for Concrete Aggregates. ASTM International, Pennsylvania, United States. doi:10.1520/C0033_C0033M-18.

[39] ASTM C31/C31M-21a. (2022). Standard Practice for Making and Curing Concrete Test Specimens in the Field. ASTM International, Pennsylvania, United States. doi:10.1520/C0031_C0031M-21A.

[40] ASTM C39/C39M-21. (2003). Standard Test Method for Compressive Strength of Cylindrical Concrete Specimens. ASTM International, Pennsylvania, United States. doi:10.1520/C0039_C0039M-21.

[41] BS EN 12390-2:2019. Testing hardened concrete. Making and curing specimens for strength tests. British Standard (BSI), London, United Kingdom.

[42] BS EN 12390-3. (2002). Testing Hardened Concrete – Part 3: Compressive Strength of Test Specimens. British Standard (BSI), London, United Kingdom.

[43] ASTM C496/C496M-17. (2017). Standard Test Method for Splitting Tensile Strength of Cylindrical Concrete Specimens. ASTM International, Pennsylvania, United States. doi:10.1520/C0496_C0496M-17.

[44] ASTM C469/C469M-22. (2002). Standard Test Method for Static Modulus of Elasticity and Poisson's Ratio of Concrete in Compression. ASTM International, Pennsylvania, United States. doi:10.1520/C0469_C0469M-22.

[45] BS EN 12390-5:2009. (2009). Testing Hardened Concrete – Part 5: Flexural Strength of Test Specimens. British Standard (BSI), London, United Kingdom.

[46] ASTM D7205/D7205M. (2011). Standard Test Method for Tensile Properties of Fiber Reinforced Polymer Matrix Composite Bars. ASTM International, Pennsylvania, United States. doi:10.1520/D7205_D7205M-06.

[47] Ali, S. I., & Allawi, A. A. (2021). Effect of Web Stiffeners on The Flexural Behavior of Composite GFRP- Concrete Beam Under Impact Load. Journal of Engineering, 27(3), 76–92. doi:10.31026/j.eng.2021.03.06.

[48] Said, A. I., & Abbas, O. M. (2023). Serviceability behavior of High Strength Concrete I-beams reinforced with Carbon Fiber Reinforced Polymer bars. Journal of Engineering, 19(11), 1515–1530. doi:10.31026/j.eng.2013.11.10.

[49] Tu, J., Zhao, Q., & Gao, K. (2022). The Design of Concrete Beams Reinforced with GFRP Bars Based on Crack Width. Materials, 15(18), 6467. doi:10.3390/ma15186467.